



저작자표시-비영리-변경금지 2.0 대한민국

이용자는 아래의 조건을 따르는 경우에 한하여 자유롭게

- 이 저작물을 복제, 배포, 전송, 전시, 공연 및 방송할 수 있습니다.

다음과 같은 조건을 따라야 합니다:



저작자표시. 귀하는 원저작자를 표시하여야 합니다.



비영리. 귀하는 이 저작물을 영리 목적으로 이용할 수 없습니다.



변경금지. 귀하는 이 저작물을 개작, 변형 또는 가공할 수 없습니다.

- 귀하는, 이 저작물의 재이용이나 배포의 경우, 이 저작물에 적용된 이용허락조건을 명확하게 나타내어야 합니다.
- 저작권자로부터 별도의 허가를 받으면 이러한 조건들은 적용되지 않습니다.

저작권법에 따른 이용자의 권리는 위의 내용에 의하여 영향을 받지 않습니다.

이것은 [이용허락규약\(Legal Code\)](#)을 이해하기 쉽게 요약한 것입니다.

[Disclaimer](#)

이학박사 학위논문

Synthesis of Graphene Quantum Dots and Antidots

그래핀 양자점과 반양자점의 합성

2016년 2월

서울대학교 대학원

화학부 물리화학 전공

박 명 진

Synthesis of Graphene Quantum Dots and Antidots

지도교수 홍 병 희

이 논문을 이학박사 학위논문으로 제출함

2015년 12월

서울대학교 대학원

화학부 물리화학 전공

박 명 진

박명진의 이학박사 학위논문을 인준함

2015년 12월

위 원 장 _____ 장두전 (인)

부위원장 _____ 홍병희 (인)

위 원 _____ 민달희 (인)

위 원 _____ 조성표 (인)

위 원 _____ 박종혁 (인)

Abstract

Synthesis of Graphene Quantum Dots and Antidots

Myung Jin Park
Department of Chemistry
Seoul National University

The Nobel prize for physics in 2010 was awarded to Professor Andrei Geim and Professor Kostya Novoselov for their topic of ‘Ground breaking experiments regarding the two-dimensional material graphene’.

The expansion of research in graphene was helped by many people who were already studying carbon nanotubes and fullerenes, simply translating their activities into this new area.

The tools for characterizing graphene is often similar to those used for nanotubes, such as transmission electron microscopy (TEM), scanning electron microscopy (SEM), electronic device fabrication, diffraction and raman spectroscopy. These similarities also give a chance for rapid advances in understanding the properties of new 2D crystals that may exhibit new behavior in graphene.

The biggest problem for fullerenes and nanotube is the manufacturing aspect. It is challenging to produce vast quantities of entirely pure materials.

Despite some of the most interesting and useful properties of fullerenes come by adding dopants or molecular functional groups, this makes their separation using high-performance liquid chromatography time consuming and thus the end product expensive.

Carbon nanotubes also suffer from the problem of mixed chiralities that lead to both semiconducting and metallic electronic transport behaviors. This has limited their application in electronics, despite demonstrating their outstanding properties at device.

Graphene, on the other hand, looks to be solving these manufacturing problems with variable synthetic methods, Chemical Vapor Deposition (CVD) and Chemical exfoliation as well. The pathway for cheap and high-quality graphene suited for a variety of applications is achievable.

Graphene is a zero-gap semiconductor since the conduction and valence bands meet at the Dirac points and exhibit a linear dispersion. The electronic density of states is zero at the Dirac points. This topology of the bands gives rise to unique and exotic electronic transport properties. The charge carriers are massless, which affects an extreme intrinsic carrier mobility. This makes graphene a promising candidate for applications in high-frequency electronics as a being more suitable than logic-based transistors.

While it is clear that outstanding properties of graphene with fascinating electronic structure that received the most attention, this intrinsic character is seen as one of the most challenging in terms of the opening the band gap.

Recently, the constricting of graphene into a finite structure has

attracted the most intensive research. A great amount of theoretical work demonstrated that the influence of band structure can be varied by edge structure and width. The first experimental results, known as a graphene nanoribbon (GNR), were patterned by electron beam lithography. The measured energy gaps were found to be inversely proportional to GNR width. However, lithographic and graphene etching resolution is limited within the sub-10nm regime.

In an attempt to solve these problems, solution processing with chemical reagents was employed to exfoliate the graphite sheets down into a narrower size, which yield GNR with a variety of shapes and repeatable uniformity.

Furthermore, graphene nanomesh as a closely related structure to GNRs has been reported; a periodic array of holes in a graphene sheet, with the necks between adjacent holes narrowing to 5nm, which provides the confinement to easily open a band gap.

The objective of this dissertation is to mainly introduce the optical properties and their applications of nanostructured graphene; graphene quantum dot (GQD) as a closely related with GNR material, and pseudo-nanomesh fabricated from catalytic etching of metal nanoparticle.

The book starts with a broad description of the graphene, which contains the atomic structure of graphene, synthetic methods, characterization using optical tool, and patterning, since these will help a general understanding of the graphene. Once an understanding of the graphene is obtained, we move towards describing each of experiments in Chapter 2 and 3.

Keyword : Graphene, Graphene Quantum dot, Graphene Nanomesh, Semiconductor, Raman spectrum of the Graphene, Optical Variation

Student Number : 2012-23043

Table of Contents

Abstract	i
Table of Contents	v
List of Figures	viii

Chapter

I . Introduction

1. The Atomic structure of Graphene	1
2. Band structure of Graphene	4
3. Synthesis Methods	
3.1 Chemical Vapor Deposition	5
3.2 Chemically exfoliated Graphite oxide	6
4. Raman spectroscopy of graphene	
4.1 Phonons in graphene	9
4.2 Electronic structure of graphene	11
4.3 Raman mode in graphene	
4.3.1 1st-order Raman mode	12
4.3.2 Divergence of the G band	13

4.3.3 2nd–order Raman mode	14
5. Nanostructured graphene patterning	
5.1 Patterning via Lithography	17
5.2 Crystallographic patterning via Catalyst	19
6. Reference	21

II. Synthesis of Graphene quantum dot and its application

1. Introduction	34
2. Experiment	36
3. Result and Discussion	37
4. Conclusion	41
5. Reference	42

III. Synthesis of Graphene Antidots

1. Introduction	55
2. Experiment	57
3. Result and Discussion	60
4. Conclusion	69

5. Reference	70
Appendix.....	91
Abstract in Korean	94

List of Figures

Chapter I

Figure 1. Atomic orbital of a carbon atom. (a). Ground state, (b) sp^3 -hybridised in diamond, (c) sp^2 -hybridised in graphene.

Figure 2. Crystal structure of graphene; (a) 2D hexagonal lattice of graphene in real space with vectors a_1 and a_2 . The unit cell is indicated in grey. It contains two nonequivalent carbon atoms A and B, each of which span a triangular sublattice as indicated with black and white atoms, respectively. (b) Reciprocal lattice with lattice vectors b_1 and b_2 . The first Brillouin zone is indicated in grey and the high symmetry points Γ , K , M are indicated. (c) Lattice planes in the real lattice.

Figure 3. Band structure of graphene. Conduction band and valence band meet at the Dirac points. Inset is a close-up of the Dirac point at small value of k , which shows the linear dispersion.

Figure 4. Optical micrographs of graphene transferred on the substrate. (a) SEM image of the multilayer graphene grown on Ni foil. (b) Optical microscope image of the monolayer graphene grown on Cu foil. (c) Optical microscope image of the overgrown graphene on the Cu foil. (d) Raman signal of the monolayer graphene.

Figure 5. Calculated phonon dispersion relation of graphene showing the

different 6-phonon branches.

Figure 6. (a) Peak shift of the G band as a function of electron concentration at 200K: (dots) measurements, (dotted line) adiabatic Born-Oppenheimer, (solid line) finite-temperature non-adiabatic calculation. (b) Full width at half maximum (FWHM) of the G band as a function of electron concentration at 200K: (dots) as measured, (line) theoretical calculation.

Figure 7. Raman spectra at values of V_{TG} between -2.2 V and $+4.0$ V. The dots are the experimental data, the black lines are fitted lorentzians, and the red line corresponds to the Dirac point. The G peak is on the left and the 2D peak is on the right.

Figure 8. Position of the G band as a function of uniaxial strain. The spectrum is measured with incident light polarized along the strain direction, collecting the scattered light with no analyser.

Figure 9. (a) Second-order raman process for the D band in graphene. (b) Second-order raman process for the 2D band. Two phonons have opposite wavevectors to conserve the total momentum in the scattering process. (c) Second-order raman process for intra valley scattering of the D' band.

Figure 10. Double resonance mechanism. (a) outer process. (b) inner process

Figure 11. SEM images of GNRs prepared by electron beam lithography.

(a) Parallel arrangement with varying diameter. (b) Arrangement with different angles. (c) Energy gap plotted as a function of the width of GNRs. (d) Graphene nanomesh fabricated by block copolymer template.

Figure 12. Anisotropic etching of graphite/graphene. (a) SEM image of channels cut by nanoparticles through a graphite surface. (b,c) STM image of nanocut graphite: typical etch orientations are along the zigzag and armchair lattice directions. (d–e) AFM image of the connected nanostructure: Etching in SLG has chirality-preserving angles of 60° and 120° , avoiding crossing of trenches leaving ~ 10 nm spacing between adjacent trenches.

Chapter II

Figure 1. Schematic of BHJ solar cell prepared by addition of three types of GQDs in BHJ layer, of which functional groups on the edge of each GQDs are tuned by reduction times.

Figure 2. XPS spectra (A) and normalized PLE and PL spectra (B) of GOQD, 5 hrs reduced GQDs, and 10 hrs reduced GQD.

Figure 3. TEM and AFM images of graphene oxide (GO) QDs (A, B), 5 hrs reduced GQDs (C, D), and 10 hrs reduced GQDs (E, F), respectively. The AFM scan ranges are $3\ \mu\text{m}\times 3\ \mu\text{m}$.

Figure 4. J–V curves (A), IPCE (B) and dark J–V curves (D) of devices with plain BHJ (black), BHJ with GOQD (red), BHJ with GQD 5 (green) or GQD 10 (blue). UV–visible adsorption spectra of GOQD and GQD 10 in chlorobenzene (C).

Figure 5. Multi–peaks fitted XPS spectra of GOQD, GQD 5 and GQD 10.

Figure 6. Height distribution (A)~(C) from AFM images in figure 3 of GOQD, GQD 5 and GQD 10.

Figure 7. J–V curves of devices prepared by addition of various concentration of GOQD (A), GQD 5 (B) and GQD 10 (C) in BHJ layers.

Figure 8. Absorption spectra of plain BHJ film (black) and BHJ films with GOQD (red) and GQD 10 (blue).

Figure 9. AFM images ($3\ \mu\text{m}\times 3\ \mu\text{m}$) of plain BHJ film (A) and BHJ films with GOQD (B), GQD 5 (C) and GQD 10 (D).

Figure 10. FT-IR spectra of GOQD, GQD 5 and GQD 10.

Table 1. Performance parameters of the devices with plain BHJ (reference) or BHJ with GOQD, GQD 5 or GQD 10.

Chapter III

Figure 1. Schematic of fabrication of nanoscale perforated graphene films. (a) Reduced graphene oxide (rGO) is coated on a SiO_2/Si substrate. (b) Diblock copolymer micelles incorporated with Pt precursors is coated on the rGO film. (c) The Pt NPs array is formed with penetration from top of rGO at 400°C in ambient condition. (d) The nanopores are formed on rGO or CVD graphene. (e) Diblock copolymer micelles incorporating with Pt precursors are first coated on the SiO_2/Si substrate. (f) The micelles film is converted into Pt NPs array after annealing at 400°C in ambient condition. (g) The CVD graphene is transferred on the Pt NPs array, followed by annealing at 400°C . (h) Local strain on graphene induced by negative thermal expansion leads to enhanced chemical reactivity resulting in localized catalytic perforation.

Figure 2. AFM and TEM images for perforation processes. (a) AFM image of uniformly coated Pt–micelle arrays on rGO. (b) AFM image of well arrayed Pt NPs, on rGO after annealing. (c) AFM image of perforated rGO after transfer to another substrate. (d) TEM image of nanopores of rGO suspended in a TEM grid. (e) AFM image of the Pt NPs array on a SiO_2/Si substrate after annealing. (f) AFM image of CVD graphene transferred on the Pt NPs array. (g) AFM image of CVD graphene subjected to local strain caused by annealing treatment. (h) AFM image of nanopores formed on CVD graphene after removing Pt

NPs. Scale bars in AFM and TEM images are 200 nm.

Figure 3. Raman analyses of CVD graphene on Pt NPs with respect to annealing time. (a) The variation of the phonon frequencies of the 2D and G modes as a function of annealing time. (b) Correlation between 2D/G intensity ratio and G mode position as a function of each annealing treated samples (Black dashed line represents second order polynomial curve fit to the data points). (c) Correlation between FWHM of G mode and its position as a function of each annealing treated samples (Black dashed line represents second order polynomial curve fit to the data points). (d) Correlation between the G and 2D modes varied by annealing. The black dashed line indicates the charge neutral graphene under randomly oriented uniaxial strain. The red solid line indicates doped graphene with varying density of holes, Green dot indicates the charge neutral and strain-free graphene. (Inset: decomposition of hole doping and strain types using unit vectors; ϵ_C : compressive strain, ϵ_T : tensile strain, e_H : hole doping effect, magenta dashed line: average value of strain-free graphene with varying density of holes.)

Figure 4. (a) AFM image of nanopores (diameter: 17 nm, spacing: 42 nm) of CVD graphene obtained from smaller molecular weight of diblock copolymer PS-P4VP (32k-13k). (b) AFM image of nanopores (diameter: 21 nm, spacing: 56 nm) of CVD graphene obtained from diblock copolymer PS-P4VP (51k-18k). (c) AFM image of nanopores (diameter: 27 nm, spacing: 125 nm) of CVD graphene obtained from higher molecular weight of diblock copolymer PS-P4VP (109k-27k). (d)

Raman spectrum with respect to each sample. (e) I_{ds} of each sample measured at constant $V_{ds}=10\text{mV}$ after the annealing under H_2/Ar atmosphere at 300°C for 10 min (solid curves) and 20 min (dashed curves).

Figure 5. (a) AFM image of annealing treated CVD graphene on Pt NPs in vacuum. (b) AFM image of annealing treated CVD graphene on silica NPs in the air. (c) AFM image of annealing treated CVD graphene on Au NPs in the air. Scale bars are 200 nm. (d) Raman spectrum with respect to each sample.

Figure 6. AFM studies of perforated of rGO. (a) AFM image of the spin-coated rGO on SiO_2/Si substrate. (b) AFM image of the arrayed Pt NPs with perforation of rGO film after annealing treatment. (c) AFM image of the Pt NPs synthesized on a bare SiO_2/Si substrate. The height histogram of Pt NPs on rGO is compared with that of the Pt NPs synthesized on a bare SiO_2/Si substrate. The height of Pt NPs on rGO is 2.4 nm smaller. This value indicates that the Pt NPs well penetrates the rGO film and resides on the SiO_2/Si substrate. Scale bars are 200 nm.

Figure 7. TEM studies of the synthesized Pt NPs. (a) TEM image of the Pt NPs synthesized using the diblock copolymer PS-P4VP (32k-13k). (b) TEM image of the Pt NPs synthesized using the diblock copolymer PS-P4VP (51k-18k). Inset represents the selected-area electron diffraction pattern of Pt NPs. (c) TEM image of the Pt NPs synthesized using the diblock copolymer PS-P4VP (109k-27k). All of the

histograms informs the size distribution with respect to each Pt NPs. Scale bars are 500 nm.

Figure 8. AFM and TEM images of perforated rGO. (a,b) Micrographs of nanopores (diameter: 8 nm, spacing: 34 nm) of rGO obtained from smaller molecular weight of diblock copolymer PS-P4VP (32k-13k). (c,d) Micrographs of nanopores (diameter: 19 nm, spacing: 101 nm) of rGO obtained from higher molecular weight of diblock copolymer PS-P4VP (109k-27k). Scale bars in AFM and TEM images are 200 nm.

Figure 9. Aggregation of the Pt NPs on CVD graphene. (a) SEM image of the large aggregation of the Pt NPs on CVD graphene forming clusters. (b) AFM image of the aggregation of the Pt NPs on CVD graphene. Scale bars in SEM and AFM images are 200 nm.

Figure 10. Surface morphology variation of CVD graphene. (a) AFM image of CVD graphene transferred on the Pt NPs array. (b) AFM image of annealing treated CVD graphene for 5 min; (c) 10 min; (d) 15 min; (e) 25 min; (f) 30 min. The ripples coexisted with suspended region are contracted, forming linear creases induced by negative thermal expansion coefficient of graphene. Localized compressive strain of graphene can act as catalytic oxidation sites for Pt NPs to decompose the chemically weakened bonding region. Scale bars are 200 nm.

Figure 11. TEM images of perforated single-layer graphene suspended in TEM grids. The single layer thickness of graphene does not give enough contrast to clearly visualize the existence of nanopores. Scale

bars, 200 nm.

Figure 12. Raman analyses of CVD graphene on Pt NPs with respect to annealing time. Correlation between FWHM of 2D mode and its position as a function of each annealing treated samples (Black dashed line represents the second order polynomial curve fit of whole data points).

Figure 13. Annealing induced Raman spectrum variation. The D and D' bands are increased proportional to annealing time, which is attributed to sp^2 bond breaking resulting in the formation of nanopore. The blue shift of the G and 2D modes is caused by strong hole doping effect during annealing in the air (Inset represent the raman spectrum variation of before and after annealing. This spectra difference can be an indicator to estimate whether the pores is formed or not).

Figure 14. Reduction of the doping concentration by the annealing process. Carrier concentration of the perforated graphene obtained from PS-P4VP (51k–18k) after the annealing at 300 °C under H_2/Ar atmosphere.

Figure 15. Photograph and SEM images for the perforation of wafer-scale graphene on the arrayed Pt NPs. Photograph and SEM images for the strain-assisted perforation of wafer-scale graphene on the arrayed Pt NPs. (a) Graphene film transferred on Pt NPs arrays on a 4-inch wafer. (b, c). Graphene on Pt NPs before annealing. (d) Perforated graphene on Pt NPs after annealing at 400° C for 30min. Scale bars are 200 nm.

Table 1. Charge density and strain in graphene on Pt NPs array as a function of annealing.

Chapter I

Introduction

1. The Atomic structure of Graphene

In order to understand the atomic structure of graphene, it is necessary to get a knowledge of the feature of elemental carbon as well as its allotropes. The overall interest in carbon is originated from the various forms of structure. This variety results from a significant electron configuration of carbon that gives a role to form different types of valence bonds to various elements, including other carbon atoms, through atomic orbital hybridization. Carbon has the atomic number 6 and therefore, electrons occupy the $1s^2$, $2s^2$, $2p_x^1$, and $2p_y^1$ atomic orbitals as illustrated in Fig. 1 (ground state). It is a tetravalent element, i.e. only the four exterior electrons participate in the formation of covalent bonds.

When forming bonds with other atoms, carbon promotes one of the $2s$ electrons into the empty $2p_z$ orbital, resulting in the hybridized orbitals. In diamond the $2s$ -energy level hybridizes with the three $2p$ levels to form four energetically equivalent sp^3 -orbitals that are occupied with one electron each (Fig. 1). The four sp^3 -orbitals are oriented with largest possible distance from each other; they therefore point towards the corners of an imaginary tetrahedron. The sp^3 -orbitals of one carbon atom overlap with the sp^3 -orbitals of other carbon atoms, forming the

3D diamond structure. The extreme rigidity of diamond is originated from the strong binding energy of the C–C sigma bonds.

In graphite, only two of the three 2p-orbitals participate in the hybridization, forming three sp^2 -orbitals (Fig. 1). The sp^2 -orbitals are oriented perpendicular to the remaining 2p-orbital, therefore lying in the X–Y plane at 120° angles. Thus, sp^2 -carbon atoms form covalent in-plane bonds having an effect on the hexagonal “honeycomb” structure of graphite. While the in-plane σ -bonds within the graphene layers (615kJ/mol) are even stronger than the C–C bonds in sp^3 -hybridised diamond (345 kJ/mol), the interplane π -bonds between layers formed by the remaining $2p_z$ -orbitals have a significantly lower binding energy, leading to an easy exfoliation of graphite along the layer plane. A single layer of graphite (graphene) has a lattice constant $a = \sqrt{3}a_0$ where $a_0 = 1.42\text{\AA}$ is the nearest neighbor interatomic distance.¹ The interplane distance between two adjacent graphene layers in AB stacked graphite is 3.35\AA .¹

The hexagonal lattice of graphene is shown in Fig. 2a with an armchair and a zigzag edge. The unit cell of graphene is a rhombus (grey) with a basis of two nonequivalent carbon atoms (A and B). The black and white circles represent sites of the corresponding A and B triangular sublattices. In Cartesian coordinates the real space basis vectors of the unit cell a_1 and a_2 are written as

$$a_1 = \begin{pmatrix} \sqrt{3}a/2 \\ a/2 \end{pmatrix} \quad \text{and} \quad a_2 = \begin{pmatrix} \sqrt{3}a/2 \\ -a/2 \end{pmatrix}$$

with $a = \sqrt{3}a_0$.² A section of the corresponding reciprocal lattice is

depicted in Fig. 2.2b together with the first Brillouin zone (grey hexagon). The reciprocal basis vectors b_1 and b_2 can be expressed as

$$b_1 = \begin{pmatrix} 2\pi/\sqrt{3}a \\ 2\pi/a \end{pmatrix} \quad \text{and} \quad b_2 = \begin{pmatrix} 2\pi/\sqrt{3}a \\ -2\pi/a \end{pmatrix}$$

and thus, the reciprocal lattice constant is $4\pi\sqrt{3}a$. The high symmetry points (Γ , M , K and K') are indicated in Fig. 2b. The reciprocal lattice is a geometrical construction that is very useful in describing diffraction data. It is an array of points where each point corresponds to a specific set of lattice planes of the crystal in real space, as illustrated in Fig. 2c.

The reciprocal lattice is generally used to depict a material's electronic band structure, plotting the bands along specific reciprocal directions within the Brillouin zone. In this context the two points K and K' (also known as Dirac point) are of particular importance. Their coordinates in reciprocal space can be expressed as

$$K = \begin{pmatrix} 2\pi/\sqrt{3}a \\ 2\pi/3a \end{pmatrix} \quad \text{and} \quad K' = \begin{pmatrix} 2\pi/\sqrt{3}a \\ -2\pi/3a \end{pmatrix}$$

(Castro Neto et al., 2009).³ Graphene is a zero-gap semiconductor since the conduction and valence bands meet at the Dirac point and exhibit a linear dispersion.⁴ This topology of the bands gives rise to unique electronic transport properties. The charge carriers are massless, which affects an extreme intrinsic carrier mobility.⁵ This makes graphene a promising candidate for applications in new generation of atomic scale thin field effect transistors.

2. The Band structure of Graphene

Each carbon atom in the graphene lattice is connected to its three nearest neighbours by strong in-plane covalent bonds. These are known as σ bond and are formed from electrons in the $2s$, $2p_x$ and $2p_y$ valence orbitals. The fourth valence electron occupies the $2p_z$ orbital which is oriented perpendicular to the plane of the graphene sheet, and as a consequence, does not interact with the in-plane σ electrons. The $2p_z$ orbitals from neighbouring atoms overlap, resulting in delocalized π (occupied or valence) and π^* (unoccupied or conduction) band. Most of the electronic properties of graphene can be understood in terms of these π band.

The calculated band structure of graphene is shown in Fig. 3. The valence and conduction band meet at the high symmetry K and K' point. In intrinsic graphene, each carbon atom contributes one electron completely filling the valence and leaving the conduction band empty. As such the Fermi level (E_f), E_f is situated precisely at the energy where the conduction and valence bands meet. These are known as the Dirac or charge neutral point.

Consideration of the dispersion relation can be limited to just two of the Dirac points (K, K') and the others are equivalent through translation by a reciprocal lattice vector. These two Dirac points in reciprocal space can be directly related to the two real space graphene sub-lattices (A, B). The region of the dispersion relation close to K, K' is plotted in the

inset to Fig. 3, showing the linear nature of the Dirac cones. The charge carriers near the Dirac point are act as massless Dirac Fermions travelling with a group velocity of $V_F \approx 1 \times 10^6 \text{ ms}^{-1}$.³

3. Synthesis Methods

3.1 Chemical Vapor Deposition

The synthesis of graphene using Chemical Vapor Deposition (CVD) method is the most promising candidates for the goal of large scale, giving a high quality crystallinity to the as prepared sample.

During synthesis using CVD, the precursor as a gas phase is injected to reaction chamber, where it react with a metal catalyst at elevated temperature and graphene is formed on the surface of the catalyst. Precursors, e.g. methane, ethylene and low molecular weight carbon based source can be used. Depending on the catalyst, two fundamental mechanisms of graphene growth are proposed.⁶ For polycrystalline Ni, the precursor is decomposed at the surface and the carbon is dissolved in the metal. When the substrate is cooled, the solubility of C in Ni decreases and graphene first segregates and then grows on the Ni surface.⁷ Consequently, it is very important to control the cooling conditions to make a monolayer graphene.⁸ An example of a few layer graphene grown on Ni is given in Fig. 4a.

However, for Cu catalyst has a totally different mechanism. The carbon intermediate is not dissolved in the metal because of the low

solubility of C in Cu even at a very high temperature (even up to 1000°C). Instead, the carbon atoms is crystalized to graphene directly on the surface at high temperature; there is no need to precisely control the cooling condition of the metal substrate. The synthesis on Cu is subjected to the surface mediated self-limiting.⁹ Once the growth of a monolayer of graphene is completed, the process is no longer propagated, because access to the catalytic Cu surface is efficiently blocked. Hence, only 1 layer of graphene would be formed by the Cu-catalyzed CVD, as shown in Fig. 4b. However, in many instances, small regions with double or multilayers, as seen in Fig. 4c, are observed. These multilayer regions may impede the fabrication of graphene based devices with a large scale due to the uniformity of the graphene films. Hence, controlling their monolayer as shown in Fig. 4b remains one of the key requirements in Cu-catalyzed CVD graphene growth.

3.2 Chemically exfoliated Graphite oxide

Owing to the surge of interest in graphene, research into various methods of production of this material has attracted scientists all over the world. Mechanical exfoliation using a commercial tape provides very high quality monolayers on substrate however it has to be isolated by time-consuming manual process. One possible solution to overcome these problems is the use of solution based methods to separate the layers of graphite by intercalation or functionalization of the individual

layers. This approach is scalable, making it applicable to the chemical functionalization.

One of the earliest investigations was reported by the B.C. Brodie who was exploring the structure of graphite by investigating the reactivity of graphite. He determined that by adding potassium chlorate (KClO_3) to a slurry of graphite in fuming nitric acid (HNO_3), the resulting material was composed of carbon, hydrogen, and oxygen, resulting in an increase of overall mass of the graphite flake. Although Brodie was unable to accurately determine the molecular weight of graphite in his studies, he had unknowingly discovered a method for oxidizing graphite. Over the years there have been numerous efforts to oxidize graphite through various modified methods but the basic principle remains the same even today.¹⁰

The Hummers method uses a combination of potassium permanganate (KMnO_4) and sulfuric acid (H_2SO_4). Although permanganate is a good established oxidizing agent, the active species in the oxidation of graphite is dimanganese heptoxide (Mn_2O_7), which appears as brownish red oil formed from the reaction of KMnO_4 with H_2SO_4 . The Mn_2O_7 is further more reactive than MnO_4^- , and is known to cause an explosive reaction when it is subjected to elevating temperatures greater than 55°C or when placed in contact with organic compounds.^{11,12} Tromel and Russ demonstrated the ability of Mn_2O_7 to selectively oxidize unsaturated aliphatic double bonds over aromatic double bonds, which may have important implications for the structure of graphite and reaction pathways during the oxidation.¹³

The exact mechanism of oxidation of graphite is unfortunately very challenging to make sure owing to the complexity of graphite's flakes and the presence of defects in those structures.

Graphite oxide obtained by this method exists in as a brown viscous slurry, which contains not only graphite oxide but also non-oxidised graphitic particles and the residues of the by-products produced during reaction. Pure graphite oxide suspensions are achieved by variable purification methods, e.g. centrifugation, dialysis which efficiently removes salts and ions.¹⁴

As prepared graphite oxide itself is insulating, its carbon framework, however, can be substantially restored by variable reduction process, thermal annealing or treatment of chemical reducing agents resulting in reduced graphite oxide.

4. Raman spectroscopy of graphene

4.1 Phonons in graphene

Over the last few decades, Raman spectroscopy has proven to be the one of ideal tools for investigation of carbon based materials. It can be possible to acquire the simultaneous information of the sample on the vibrational structure as well as on the electronic properties of materials. Moreover, it is a fast, reliable and nondestructive method delivering results with high precision and resolution.

The unit cell of graphene contains two atoms, A and B. In total, six phonon dispersion branches can be constructed out of the two atoms. Three modes whose energy tends to zero at the center of 1st brillouin zone are denoted as acoustic phonons and the other three with a finite energy are optical phonon branches. For both the optical and acoustic branches, two phonons are transverse and one longitudinal with respect to the direction of phonon propagation given by the wavevector, q in the two-dimensional honeycomb lattice, the direction of propagation is usually chosen parallel to the nearest carbon-carbon direction, e.g. between the sub-lattices (A and B) in the graphene. For the longitudinal phonons, the atomic displacements are parallel to the phonon propagation, whereas they are perpendicular for the transverse phonons.

The atomic displacements of the two transverse phonons are also perpendicular to each other. In a two-dimensional lattice of graphene, this means that a longitudinal and one transverse phonon are in-plane vibrations and the other transverse phonon vibrates in the direction perpendicular to the graphene layer (out of plane). The two in-plane longitudinal modes are denoted as LA (longitudinal acoustic) and LO (longitudinal optical) phonons. The four transverse phonons are assigned to in-plane transverse acoustic (iTA), in-plane transverse optic (iTO), out-of-plane transverse acoustic (oTA) and out-of-plane transverse optic (oTO) branches, respectively. This classification of the phonons holds for high symmetry $\Gamma - K$ and $\Gamma - M$ directions within the Brillouin zone. The calculated phonon dispersion relation is shown in Fig. 5.¹⁵

Phonons can also be classified according to representations of a point group to which the unit cell of graphene belongs. The symmetry of monolayer graphene (MLG) follows the point group D_{6h} which is the symmetry of the wave-vector at the center of the Brillouin zone (Γ point) in the reciprocal space. The six normal modes of single layer graphene are transformed in the Γ point according to the E_{2g} , B_{2g} , E_{1u} and A_{2u} representations of the D_{6h} point group. Two modes (E_{2g} and E_{1u}) are doubly degenerated and other two are non-degenerated. E_{2g} and B_{2g} are optical modes and E_{1u} and A_{2u} are acoustic modes. The only Raman active mode is E_{2g} and the corresponding line is called the G band in the graphene Raman spectrum. The double degeneracy of the mode is the consequence of the fact that the iTO and LO branches meet exactly at

the Γ point. This degeneracy is lifted for points inside the Brillouin zone as can be seen in Fig. 5 for the LO and iTO branches outside the Γ point in the Γ -K direction.

In addition, phonons near the K-point give a significant contribution to the graphene Raman spectrum. There are two optical phonons exactly at the K-point, one coming from the iTO branch and another from the combination of the iLO and iLA branches. The former belongs to a Raman active A_1 representation of the point group D_{3h} . For the totally symmetric A_1 mode, all the six atoms in a hexagonal ring vibrate in a radial direction. The corresponding Raman line is called as the D band.

4.2 Electronic structure of graphene

The first Brillouin zone of graphene is a hexagon with high symmetry points Γ at the center of the first Brillouin zone (1st BZ) and two inequivalent points K and K' in the corners. Each carbon atom has three bonds in the plane and one orbital perpendicular to the plane. Electrons from the perpendicular orbitals form band close to the Fermi level represented as π and π^* bands. In the band structure of monolayer graphene, the π band corresponds to the valence band and the π^* band is the conduction band. The bands meet each other at the corners of the 1st BZ, the so called Dirac points. The Fermi level is at the Dirac points and the energy scale of the bands is given as ($\gamma_0 \approx 3\text{eV}$) acquired from the condition in zero temperature and no doping. This

means that the linear dispersion of the valence and conduction band is sufficient for analyzing raman experiments performed with lasers in the visible range.

4.3 Raman mode in graphene

4.3.1 1st-order Raman mode

The G band at around 1583cm^{-1} is the only Raman active first-order mode in monolayer graphene. Its line position and line width strongly depend on the doping state. This dependence is demonstrated experimentally in Fig. 6 for an electrically gated graphene sample.¹⁶ The G band upshifts when a positive gate voltage is applied and the sample is electron doped. The line width decreases with the doping (Fig.6, right). The trend is also similar for hole doping despite a smaller range of doping. The solid line in both panels is a calculation taking into account the non-adiabatic effects. It follows the experimental result well in particular for the line position. The logarithmic divergence is smeared out in the experiment owing to local temperature effects and inhomogeneous doping of the graphene surface. The importance of going beyond the common Born–Oppenheimer approximation is demonstrated by the dotted line in Fig. 6 (left). It is a result of a calculation that does not take the dynamic effects into account and its disagreement with the

experimental results is obvious.

The experiment that offers much higher doping levels is the electrochemical top gating method.¹⁷ The dependence of the G band position and the line width (FWHM) is shown in Fig. 7. The doping range is one order of magnitude larger than measurements given by Pisana et al.¹⁶ The results of both experiments are in qualitative agreement.

In this wider range, the theory of Lazzeri and Mauri¹⁸ still takes the experimental trends such as the asymmetry between electrons and holes, but the deviation from the experiment becomes significant at high doping levels. The asymmetry between the electron and hole doping is clear with smaller values of the doping induced shift. The doping removes or adds electrons from the system and changes the carbon-carbon bond strength.¹⁹ Hole doping increases the strength and therefore hardens the G band frequency. Electron doping does not the same role significantly. Both effects are superimposed on the frequency change owing to electron-phonon coupling. For hole doping, the effect of both mechanisms is cumulative whereas they act against each other for electron doping. Therefore, the frequency shift owing to electron doping is not as large as that for hole doping.

4.3.2 Divergence of the G band

The degeneracy of the G band at the Γ -point can be lifted by applying uniaxial strain.²⁰ The G band splits into two components that

redshift linearly with the increasing strain as shown in Fig. 8. However, the rate of the redshift is different for the two lines. The reason is that the phonon eigenvectors that give rise to the two Raman components are not equivalent under the applied strain. The component where the wavevector is perpendicular to the strain is less affected and has a higher energy than the line with the phonon eigenvector parallel to the strain. The relative intensities of the Raman components change with polarization of the incident laser light allowing a probe of the sample crystallographic orientation with respect to the strain direction. A universal plot relating the shift of the G band to the strain can be made for graphene. This can show the construction of correlation between Raman shift and strain.²¹

4.3.3 2nd-order Raman mode

The D band at $\sim 1300\text{cm}^{-1}$ and 2D band at $\sim 2690\text{cm}^{-1}$ are known in all carbon base materials. Looking at the phonon dispersion, it is obvious that the D band can be ascribed to iTO-derived phonon near the K point of the Brillouin zone and the 2D band is its overtone. The origin of the behavior was recognized as being the result of double resonance process, which exhibit a dispersive behavior.²²

There are several mechanism for elucidating the phonon relationship. First, the electron in the initial state i with the wavevector k near the K point is excited to the conduction band by absorbing a photon with the

energy E_1 (Fig. 9).⁶ After that, Several scattering for the electron can be generated. For the D band, the electron emits a phonon with a wavevector q and phonon frequency (ω_{ph}) and moves to the K' point (state b). The electron is then back scattered by a defect to the state c. The backscattering changes the electron momentum by $-q$. The electron recombines with the hole in the state i, which emit a photon with the scattered energy (E_s).

The scattering of an electron between K and K' points is said to be an 2D band as an intervalley scattering (Fig. 9b). The magnitude q of the phonon wavevector involved follows $q \approx 2k$, where k is the electron wavevector. This condition is imposed by momentum conservation and both wavevectors are measured from the K point. The electronic state with a particular wavevector k can be selected by laser energy (E_{laser}). By changing E_{laser} , the phonon energy also changes and follows the dispersion of the iTO derived branch in the vicinity of the K point. Because the branch has a local minimum at the K point, the position of both the D and 2D bands always increases as a function of increasing (E_{laser}).

For the scattering process discussed so far it was assumed that the exchanged momentum, q , connects the outer parts of the Dirac cones at the K and K' points. In addition, the process connecting the inner parts is also possible. The principle is demonstrated in Fig. 10.²⁴

Both processes contribute to the shape of the D and the 2D bands of graphene. The outer process due to the phonons from the $\Gamma-K$ are combined with the inner scattering. Because the phonon branches in the

two directions are generally different, the 2D band is splitted into two components even at zero strain. The splitting becomes more pronounced under uniaxial strain. The symmetry of a graphene lattice lowers and the electronic bands change differently along different directions in the BZ. Depending on which strain direction the electron is scattered within 1st BZ, phonons with different q vectors take part in the double resonance process.

Not only does the intervalley scattering participate in electronic transition, intravalley electronic transitions are also possible. The electron is scattered in the bands of the same K point. The momentum exchange in the process is small and the corresponding phonon comes from the LO derived branch near the Γ point. Owing to the over bending of the branch, the phonon from defect scattering in Fig. 9c leads to a higher band energy than the G band in the spectrum. It is called the D' band and assigned at around 1620cm^{-1} . However, its intensity is significantly smaller than that for the G band.

The dependence of the peak position and intensity on doping was investigated by Das et al.¹⁷ and Kalbac et al.²⁵ for the 2D band. For electron doping, the peak position does not considerably change at low doping levels. At higher doping stages, however, the line position redshifts by $\sim 20\text{cm}^{-1}$ for electron doping and it is blueshifted by the same amount for hole doping. Doping has an important role in peak position, which changes the equilibrium lattice parameters; electron doping results in expansion of the lattice giving rise to softening of the 2D mode whereas hole doping induces contraction of the lattice and

phonon stiffening.

5. Nanostructured graphene

5.1 Patterning via Lithography

The gapless band structure of graphene makes it difficult for the direct use in graphene based field effect transistors, which is one of the most extensively discussed topics in graphene electronics. Therefore, in order to give a semiconducting property to graphene, it will be necessary to produce graphene nanoribbons (GNR) with widths below 10nm.²⁶

Fabrication of GNRs with a sufficiently small width for opening a band gap was first achieved by means of electron beam lithography.²⁷ Mechanically exfoliated graphene was patterned by electron beam lithography and then exposed to oxygen plasma. The electron beam resist served as an etching mask. In Fig. 11a,b SEM images of parallel GNRs with varying width oriented along the same crystallographic

direction of the graphene layer is shown. GNRs with widths ranging from 10 to 100nm have been fabricated.²⁸ In Fig. 11c, the energy gap (E_{gap}) is plotted as a function of the GNR width (W). This plot shows clearly that the energy gap is inversely proportional to the ribbon width. Nanoribbons with a width of $\approx 15\text{nm}$ exhibit energy gaps of up to $\approx 0.2\text{eV}$. In the inset, the energy gap is plotted as a function of the relative angle (θ) for devices fabricated along different orientations on the graphene sheet (Fig. 11b). These values appear to be randomly scattered, not showing any sign of crystallographic directional dependence. This finding suggests that the edge structure is not well defined. Although it has been demonstrated that electron beam lithography can be a tool to pattern GNRs, the study on opening a band gap originated from transverse electron confinement in the defined edge structure should be more evolved.

GNRs with sub-10nm width can also be prepared by means of nanowire lithography.²⁹ In this process chemically synthesized silicon nanowires are deposited onto graphene and used as the physical protection mask during an oxygen plasma treatment acting as an etching process. The GNR width can be controlled by varying nanowire diameter and etching time. GNRs with widths down to 6nm have been fabricated in this way. Therefore, nanowire lithography shows the potential to create interesting graphene nanostructures with sub-10nm measures. However, a challenge lies in controlling the deposition of the nanowire masks on the graphene layer. For large-scale parallel device integration, a deposition method with positional and directional control will be required.

An inverse structure, graphene nanomesh, can be also generated by means of block copolymer lithography (Fig. 11d).³⁰ The graphene nanomesh is created using a self assembled block copolymer with a periodic cylindrical domain arrangement as an etching mask. Neck widths as small as ≈ 7 nm have been achieved. A different method that has been employed to fabricate graphene nanomeshes with widths below 10nm is nanoimprint lithography.³¹

5.2 Crystallographic patterning via Catalyst

Graphene can be patterned by means of catalytic hydrogenation and catalytic oxidation reactions. This approach involves the dispersion of catalytic nanoparticles on a graphite or graphene sheet and the subsequent exposure to hydrogen or oxygen at elevated temperatures. The thermally activated nanoparticles start to act like ‘knives’, cutting trenches along specific crystallographic directions of the graphene or graphite surface.^{32, 33, 34, 35}

As a first step of the catalytic hydrogenation reaction, the catalytic particle, typically Fe, Ni or Co, dissociates molecular hydrogen. Atomic hydrogen then diffuses to the graphene edge, where it reacts with carbon to form methane from bond breaking of double bond. In this way, all catalytic particles that lie at a graphene edge eat up graphitic carbon

starting from that edge and produce etched channels with widths equal to the particle size.

Fig. 12a shows an SEM image of a HOPG surface where nanosize nanoparticles have etched channels under the thermal treatment at 1000°C in Ar/H₂ condition. Several straight channels have been formed. Each of them starts from a graphite step edge, which demonstrates that an edge is necessary to initiate the etching process. In Fig. 12b, an STM image is shown where the etching directions are accomplished, which determined through comparison with the crystallographic orientation of the graphene flake in the high resolution STM image in Fig. 12c. Interestingly, channels with widths of more than 10nm appear to be parallel to a zigzag direction, whereas narrower channels are predominantly aligned with an armchair direction.³² This observation suggests that patterning of graphene with structurally defined edge termination can be achieved via catalytic hydrogenation.

The formation of sub-10nm GNRs by means of this approach has been reported by Campos et al. (2009).³⁶ The authors carried out catalytic hydrogenation experiments on monolayer graphene using Ni nanoparticles as catalyst. They found that when a nanoparticle gets into close vicinity ($\approx 10\text{nm}$) of a previously etched trench, it is deflected before reaching the trench. Moreover, they observed trenches where the catalytic particle first approaches another trench and is then deflected to continue etching in a direction parallel to the other trench that results in the formation of GNRs with widths of 10nm and below (Fig.12d,e). This approach opens up a possibility of orientation controlled graphene

patterning without metal mediated contamination.

6. Reference

1. Haering, R. R., Band Structure of rhombohedral graphite. *Canadian Journal of Physics* **1958**, *36* (3), 352–362.
2. Dresselhaus, M. S.; Dresselhaus, G.; Saito, R., Physics of carbon nanotubes. *Carbon* **1995**, *33* (7), 883–891.
3. Castro Neto, A. H.; Guinea, F.; Peres, N. M. R.; Novoselov, K. S.; Geim, A. K., The electronic properties of graphene. *Reviews of Modern Physics* **2009**, *81* (1), 109–162.
4. Novoselov, K. S.; Geim, A. K.; Morozov, S. V.; Jiang, D.; Katsnelson, M. I.; Grigorieva, I. V.; Dubonos, S. V.; Firsov, A. A., Two-dimensional gas of massless Dirac fermions in graphene. *Nature* **2005**, *438* (7065), 197–200.

5. Morozov, S. V.; Novoselov, K. S.; Katsnelson, M. I.; Schedin, F.; Elias, D. C.; Jaszczak, J. A.; Geim, A. K., Giant Intrinsic Carrier Mobilities in Graphene and Its Bilayer. *Physical Review Letters* **2008**, *100* (1), 016602.
6. Li, X.; Cai, W.; Colombo, L.; Ruoff, R. S., Evolution of Graphene Growth on Ni and Cu by Carbon Isotope Labeling. *Nano Letters* **2009**, *9* (12), 4268–4272.
7. Shelton, J. C.; Patil, H. R.; Blakely, J. M., Equilibrium segregation of carbon to a nickel (111) surface: A surface phase transition. *Surface Science* **1974**, *43* (2), 493–520.
8. Reina, A.; Jia, X.; Ho, J.; Nezich, D.; Son, H.; Bulovic, V.; Dresselhaus, M. S.; Kong, J., Large Area, Few-Layer Graphene Films on Arbitrary Substrates by Chemical Vapor Deposition. *Nano Letters* **2009**, *9* (1), 30–35.
9. Li, X.; Cai, W.; An, J.; Kim, S.; Nah, J.; Yang, D.; Piner, R.; Velamakanni, A.; Jung, I.; Tutuc, E.; Banerjee, S. K.; Colombo, L.; Ruoff, R. S., Large-Area Synthesis of High-Quality and Uniform Graphene Films on Copper Foils. *Science* **2009**, *324* (5932), 1312–1314.
10. Brodie, B. C., On the Atomic Weight of Graphite. *Philosophical Transactions of the Royal Society of London* **1859**, *149*, 249–259.
11. Simon, A.; Dronskowski, R.; Krebs, B.; Hettich, B., The Crystal

Structure of Mn_2O_7 . *Angewandte Chemie International Edition in English* **1987**, *26* (2), 139–140.

12. Koch, K. R., Oxidation by Mn_2O_7 : An impressive demonstration of the powerful oxidizing property of dimanganeseheptoxide. *Journal of Chemical Education* **1982**, *59* (11), 973.
13. Trömel, M.; Russ, M., Dimanganheptoxid zur selektiven Oxidation organischer Substrate. *Angewandte Chemie* **1987**, *99* (10), 1037–1038.
14. Eda, G.; Fanchini, G.; Chhowalla, M., Large–area ultrathin films of reduced graphene oxide as a transparent and flexible electronic material. *Nat Nano* **2008**, *3* (5), 270–274.
15. Ferrari, A. C.; Basko, D. M., Raman spectroscopy as a versatile tool for studying the properties of graphene. *Nat Nano* **2013**, *8* (4), 235–246.
16. Pisana, S.; Lazzeri, M.; Casiraghi, C.; Novoselov, K. S.; Geim, A. K.; Ferrari, A. C.; Mauri, F., Breakdown of the adiabatic Born–Oppenheimer approximation in graphene. *Nat Mater* **2007**, *6* (3), 198–201.
17. DasA; PisanaS; ChakrabortyB; PiscanecS; Saha, S. K.; Waghmare, U. V.; Novoselov, K. S.; Krishnamurthy, H. R.; Geim, A. K.; Ferrari, A. C.; Sood, A. K., Monitoring dopants by Raman scattering in an electrochemically top–gated graphene transistor. *Nat Nano* **2008**, *3*

- (4), 210–215.
18. Lazzeri, M.; Mauri, F., Nonadiabatic Kohn Anomaly in a Doped Graphene Monolayer. *Physical Review Letters* **2006**, *97* (26), 266407.
 19. Yan, J.; Zhang, Y.; Kim, P.; Pinczuk, A., Electric Field Effect Tuning of Electron–Phonon Coupling in Graphene. *Physical Review Letters* **2007**, *98* (16), 166802.
 20. Mohiuddin, T. M. G.; Lombardo, A.; Nair, R. R.; Bonetti, A.; Savini, G.; Jalil, R.; Bonini, N.; Basko, D. M.; Galiotis, C.; Marzari, N.; Novoselov, K. S.; Geim, A. K.; Ferrari, A. C., Uniaxial strain in graphene by Raman spectroscopy: G peak splitting, Grüneisen parameters, and sample orientation. *Physical Review B* **2009**, *79* (20), 205433.
 21. Frank, O.; Tsoukleri, G.; Riaz, I.; Papagelis, K.; Parthenios, J.; Ferrari, A. C.; Geim, A. K.; Novoselov, K. S.; Galiotis, C., Development of a universal stress sensor for graphene and carbon fibres. *Nat Commun* **2011**, *2*, 255.
 22. Thomsen, C.; Reich, S., Double Resonant Raman Scattering in Graphite. *Physical Review Letters* **2000**, *85* (24), 5214–5217.
 23. Das, A.; Chakraborty, B.; Sood, A. K., Probing single and bilayer graphene field effect transistors by raman spectroscopy. *Modern Physics Letters B* **2011**, *25* (08), 511–535.

24. Mohr, M.; Maultzsch, J.; Thomsen, C., Splitting of the Raman 2D band of graphene subjected to strain. *Physical Review B* **2010**, *82* (20), 201409.
25. Kalbac, M.; Reina-Cecco, A.; Farhat, H.; Kong, J.; Kavan, L.; Dresselhaus, M. S., The Influence of Strong Electron and Hole Doping on the Raman Intensity of Chemical Vapor-Deposition Graphene. *ACS Nano* **2010**, *4* (10), 6055–6063.
26. Barone, V.; Hod, O.; Scuseria, G. E., Electronic Structure and Stability of Semiconducting Graphene Nanoribbons. *Nano Letters* **2006**, *6* (12), 2748–2754.
27. Chen, Z.; Lin, Y.-M.; Rooks, M. J.; Avouris, P., Graphene nanoribbon electronics. *Physica E: Low-dimensional Systems and Nanostructures* **2007**, *40* (2), 228–232.
28. Han, M. Y.; Özyilmaz, B.; Zhang, Y.; Kim, P., Energy Band-Gap Engineering of Graphene Nanoribbons. *Physical Review Letters* **2007**, *98* (20), 206805.
29. Bai, J.; Duan, X.; Huang, Y., Rational Fabrication of Graphene Nanoribbons Using a Nanowire Etch Mask. *Nano Letters* **2009**, *9* (5), 2083–2087.
30. Bai, J.; Zhong, X.; Jiang, S.; Huang, Y.; Duan, X., Graphene nanomesh. *Nat Nano* **2010**, *5* (3), 190–194.

31. Liang, X.; Jung, Y.-S.; Wu, S.; Ismach, A.; Olynick, D. L.; Cabrini, S.; Bokor, J., Formation of Bandgap and Subbands in Graphene Nanomeshes with Sub-10 nm Ribbon Width Fabricated via Nanoimprint Lithography. *Nano Letters* **2010**, *10* (7), 2454–2460.
32. Ci, L.; Xu, Z.; Wang, L.; Gao, W.; Ding, F.; Kelly, K.; Yakobson, B.; Ajayan, P., Controlled nanocutting of graphene. *Nano Res.* **2008**, *1* (2), 116–122.
33. Datta, S. S.; Strachan, D. R.; Khamis, S. M.; Johnson, A. T. C., Crystallographic Etching of Few-Layer Graphene. *Nano Letters* **2008**, *8* (7), 1912–1915.
34. Severin, N.; Kirstein, S.; Sokolov, I. M.; Rabe, J. P., Rapid Trench Channeling of Graphenes with Catalytic Silver Nanoparticles. *Nano Letters* **2009**, *9* (1), 457–461.
35. Schäffel, F.; Warner, J.; Bachmatiuk, A.; Rellinghaus, B.; Büchner, B.; Schultz, L.; Rummeli, M., Shedding light on the crystallographic etching of multi-layer graphene at the atomic scale. *Nano Res.* **2009**, *2* (9), 695–705.
36. Campos, L. C.; Manfrinato, V. R.; Sanchez-Yamagishi, J. D.; Kong, J.; Jarillo-Herrero, P., Anisotropic Etching and Nanoribbon Formation in Single-Layer Graphene. *Nano Letters* **2009**, *9* (7), 2600–2604.

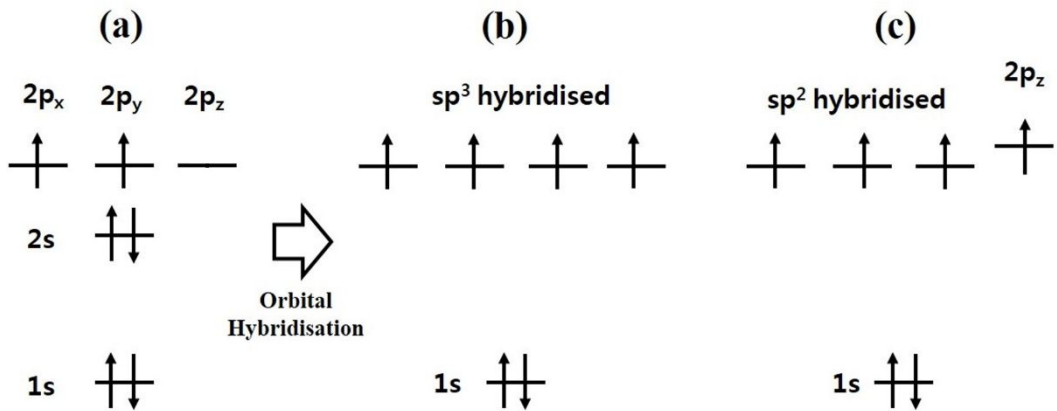


Figure 1. Atomic orbital of a carbon atom. (a). Ground state, (b) sp^3 -hybridised in diamond, (c) sp^2 -hybridised in graphene.

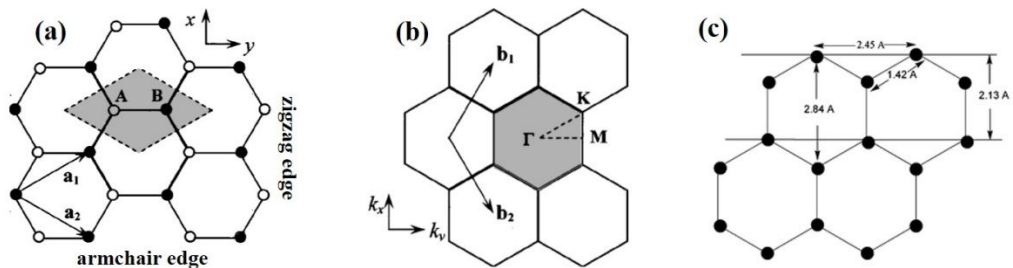


Figure 2. Crystal structure of graphene; (a) 2D hexagonal lattice of graphene in real space with vectors a_1 and a_2 . The unit cell is indicated in grey. It contains two nonequivalent carbon atoms A and B, each of

which span a triangular sublattice as indicated with black and white atoms, respectively. (b) Reciprocal lattice with lattice vectors b_1 and b_2 . The first Brillouin zone is indicated in grey and the high symmetry points Γ , K , M are indicated. (c) Lattice planes in the real lattice.

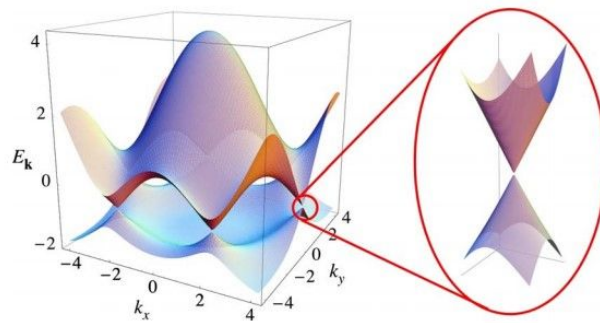


Figure 3. Band structure of graphene. Conduction band and valence band are touched at the Dirac points. Inset is a close-up of the Dirac point at small value of k , which shows the linear dispersion.

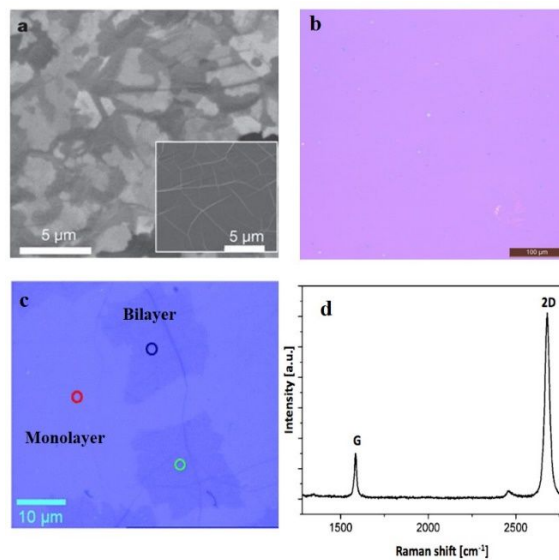


Figure 4. Optical micrographs of graphene transferred on the substrate. (a) SEM image of the multilayer graphene grown on Ni foil. (b) Optical microscope image of the monolayer graphene grown on Cu foil. (c) Optical microscope image of the over grown graphene on the Cu foil. (d) Raman signal of the monolayer graphene.

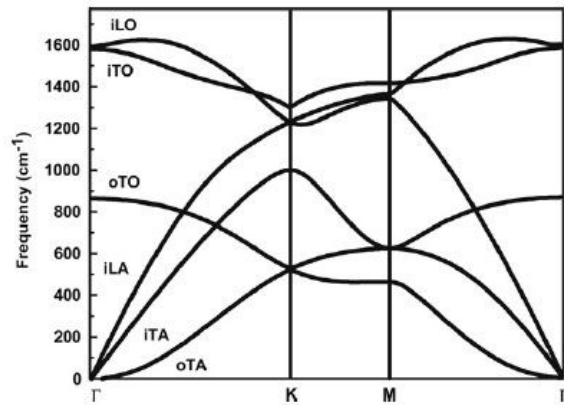


Figure 5. Calculated phonon dispersion relation of graphene showing the different 6-phonon branches.

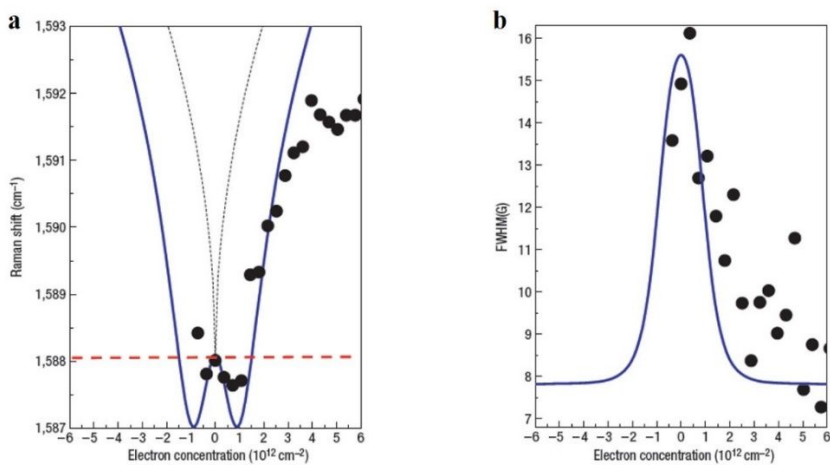


Figure 6. (a) Peak shift of the G band as a function of electron

concentration at 200K: (dots) measurements, (dotted line) adiabatic Born–Oppenheimer, (solid line) finite–temperature non–adiabatic calculation. (b) Full width at half maximum (FWHM) of the G band as a function of electron concentration at 200K: (dots) as measured, (line) theoretical calculation.

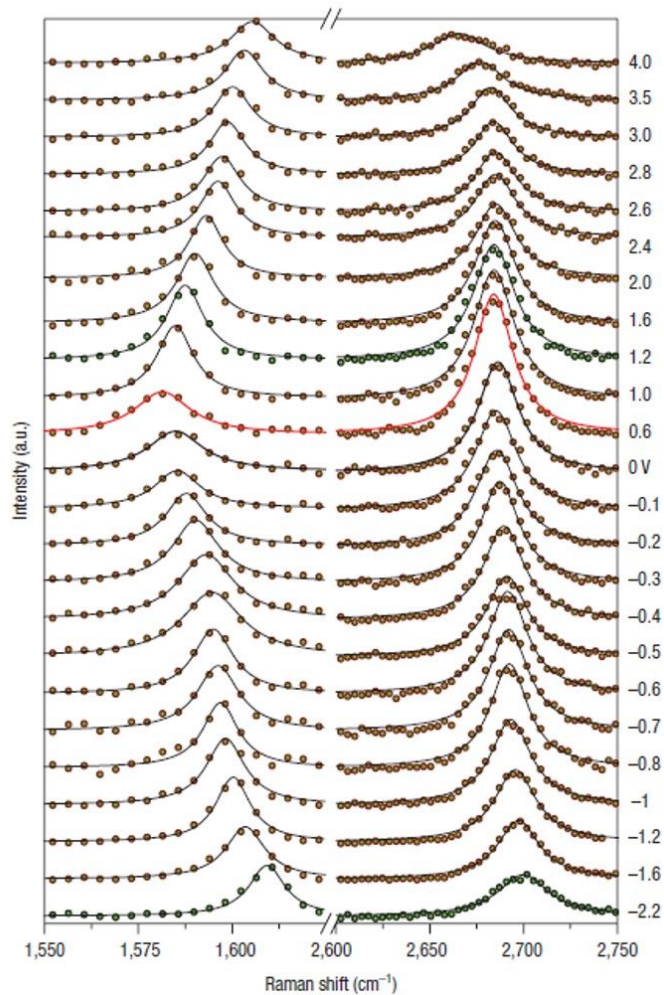


Figure 7. Raman spectrum of graphene at values of V_{TG} between -2.2 V and $+4.0$ V. The dots are the experimental data, the black lines are fitted lorentzians, and the red line corresponds to the Dirac point. The G peak

is on the left and the 2D peak is on the right.

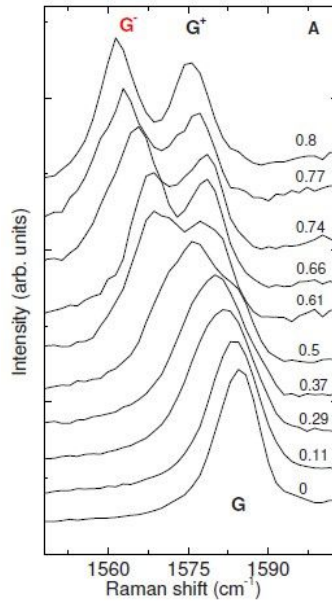


Figure 8. Position of the G band as a function of uniaxial strain. The spectrum is measured with incident light polarized along the strain direction, collecting the scattered light with no analyser.

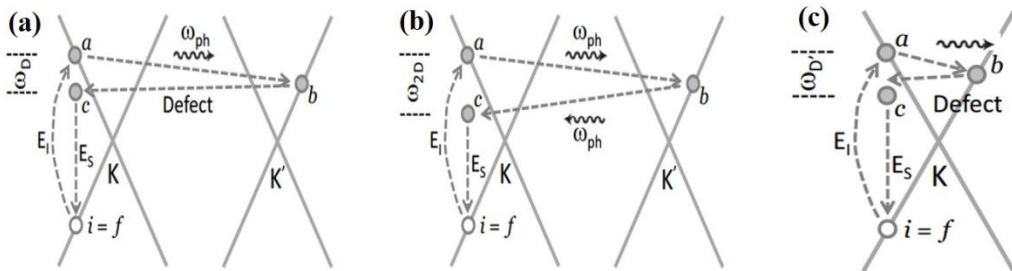


Figure 9. (a) Second-order raman process for the D band in graphene. (b) Second-order raman process for the 2D band. Two phonons have opposite wavevectors to conserve the total momentum in the scattering process. (c) Second-order raman process for intra valley scattering of the D' band.

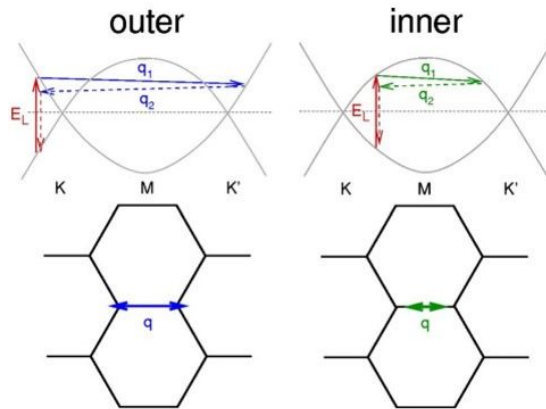


Figure 10. Double resonance mechanism. (a) outer process. (b) inner process

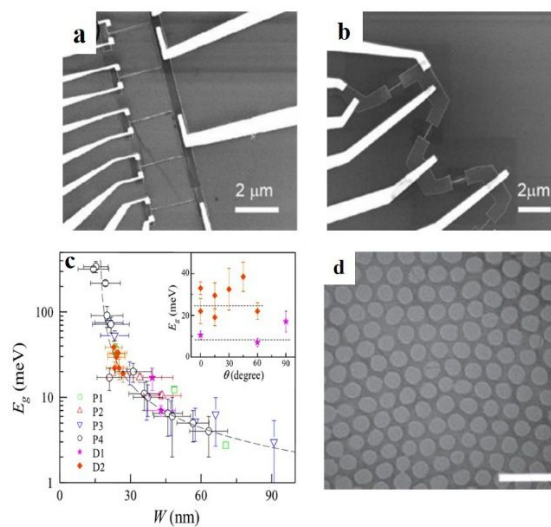


Figure 11. SEM images of GNRs prepared by electron beam lithography. (a) Parallel arrangement with varying diameter. (b) Arrangement with different angles. (c) Energy gap plotted as a function of the width of GNRs. (d) Graphene nanomesh fabricated by block copolymer template (scale bar: $2 \mu\text{m}$).

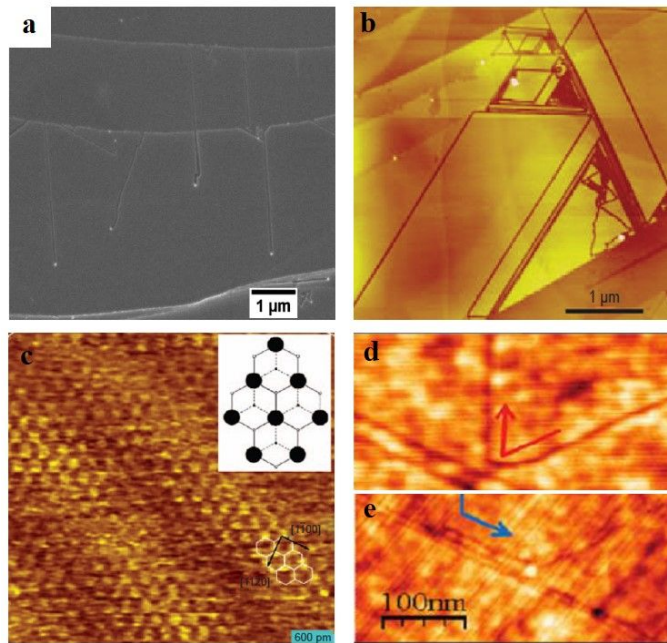


Figure 12. Anisotropic etching of graphite/graphene. (a) SEM image of channels cut by nanoparticles through a graphite surface. (b,c) STM image of nanocut graphite: typical etch orientations are along the zigzag and armchair lattice directions. (d–e) AFM image of the connected nanostructure: Etching in graphene has chirality-preserving angles of 60° and 120° , avoiding crossing of trenches leaving ~ 10 nm spacing between adjacent trenches.

Chapter II

Synthesis of Graphene quantum dot and its application

1. Introduction

Organic photovoltaic devices (OPVs) based on the bulk–heterojunction (BHJ) structure with a blend of polymer donor and fullerene acceptor have been considered as one of the next–generation solar cells due to their possible applications for flexible devices and large area photovoltaics.^{1–5} However, the poor carrier mobility of the BHJ materials usually restrict the thickness of the BHJ film because the recombination of the carriers is directly proportional to the film thickness.^{6–8} In recent years, a lot of researches have been instigated to improve the power conversion efficiency (PCE) of the OPVs with the restricted film thickness, exploiting the synthesis of newly designed polymer or small molecules, the modification of morphologies, the plasmon or light

scattering using nano-patterned structures, and the novel interlayers as electron or hole conductors.⁹⁻¹⁹ Particularly, the addition of metal nanoparticles such as Ag or Au into the OPVs shows considerable improvements in the device performance due to the localized surface plasmon resonances (LSPR) and the incident light scattering or reflection.²⁰⁻²⁴ In addition, the device resistance (series or shunt resistance) characteristics can also be improved by mixing the metal nanoparticles in the active layer.^{24,25} As alternative approaches, various inorganic nanomaterials including nanoparticles, nanorods, and quantum dots have been exploited as the acceptor materials of the BHJ thin film or hybrid solar cells, improving both the light absorption and the electrical property of the BHJ layers.²⁶⁻²⁸ However, these alternative materials are hard to synthesize and usually not environmentally friendly. Moreover, the metal nanoparticles embedded BHJ layers often cause a short circuit leading to permanent damage.

Recently, it was reported that a newly emerging material, graphene quantum dots (GQDs), is useful for optoelectronic applications owing to its tunable band-gap property depending on size and chemical functionality, which is important to improve the efficiency of optoelectronic devices.^{31,32} Moreover, the good dispersity of GQDs in common solvents is expected to enable various solution-processible applications.³³⁻⁴⁰ The amount of sp^2 carbon in GQDs can be controlled by varying reduction time, which is useful for optimizing the electrical and optical properties.³⁵ Thus, we controlled the degree of oxidation with maintaining other parameters constant, and found that there is a

compromise between short-circuit current (J_{sc}) and fill factors (FF). These values cannot be maximized at the same time, but the optimized reduction condition yields the power conversion efficiency (PCE) superior to a reference device without GQDs.

2. Experiment

1. Synthesis of oxidized graphene quantum dots

GOs were synthesized by the modified Hummer's method.⁵⁴ To make small and uniformly sized RGO powder, the purified GO was subjected to thermal reduction (250°C, 2hrs) inside a box furnace.⁵⁵ The 0.5g of reduced GO (RGO) powder was added to the mixture of sulfuric acid and nitric acid, and mildly sonicated for 24 hours. To remove the acidic ingredients in the solution, the sample was diluted in distilled water after centrifuging for 30 min at 4000 rpm. This rinsing process was repeated for 6 times. The sample was mildly sonicated for 24 hours, and filtrated through 0.02 nm nanoporous anodisk. The resulting filtrate was further purified overnight using a 3500 Da dialysis bag.

2. Synthesis of reduced graphene quantum dots

The oxidized RGO dispersed in water was placed in small pressure vessel (Model No. CV100 II-sin Autoclave) and was subjected to hydrothermal reduction at 200°C for 5 hrs and 10 hrs, respectively. The

reduced GQDs were filtered using a 0.02 μm nanoporous anodisk. The Brown filtrate was further filtered by a 3500Da dialysis bag overnight.

3. Fabrication of OPVs

The BHJ devices composed of PTB7/PC71BM with blended GOQD (oxidized GQDs), GQD 5 (reduced GQDs for 5hrs), and GQD 10 (reduced GQDs for 10hrs) are prepared. A 40 nm thick hole conducting layer was deposited by spin casting PEDOT:PSS (AI4083, Clevious) on a pre-cleaned ITO glass, and then dried at 150 °C for 15min. A ~80nm thick layer of BHJ was spin-coated on top of the PEDOT:PSS layer in an Ar filled glove box. The BHJ was prepared to 2.5wt% in chlorobenzene solution mixed with 3% of 1,8-diiodooctane. The blend ratio of PTB7 (1-material Chemscitech Inc.) and PC71BM (Nano-c) was 1:1.5 in weight. To optimize the concentration of GQDs in BHJ, GQDs were mixed with the BHJ solution at different weight ratios from 0.01% to 0.80%. Then, a ~6 nm thick TiOx interlayer was spin-coated as an electron conducting layer.⁵⁶ Finally, a 100nm thick Al cathode was thermally evaporated at $\sim 10^{-7}$ Torr.

3. Result and Discussion

In this study, we synthesized three different types of GQDs with different oxidation degrees as shown in Figure 1: oxidized graphene

quantum dots (GOQD); 5 hrs reduced GQDs (GQD 5); and 10 hrs reduced GQDs (GQD 10). We didn't consider further reduction because it tends to saturate after ~10 hrs. We added the GQDs to the BHJ OPVs with PTB7:PC71BM, and found that the positive effect of GQDs varies with the reduction time of GQDs, where J_{sc} increases with oxidation but FF increases with reduction. This indicates that the improved PCE of GQD-embedded OPV devices is relevant to the charge-carrier transportation and the light-absorption ability of the different GQDs. The 5 hrs reduced GQDs resulted in the increased power conversion efficiency from 6.70 % to 7.60 %.

GOs possess large amount of oxygen based functional groups with sp^2 and sp^3 hybridization.^{41,42} In oxidative conditions, the oxygen atoms tend to form a sp^3 bond with carbons by breaking C=C bonds, resulting in sp^3 -hybridized epoxy chain structures.⁴³ Further oxidation leads to the formation of epoxy pairs, carbonyl groups, and hydroxyl groups at the edge sites of GOs.⁴⁴ As a result, the size of GOs decreases during the consecutive oxidation processes, while the sp^2 - sp^3 carbon ratio is maintained.⁴⁵ In the hydrothermal reduction process, the oxygen-related functional groups are gradually removed,^{35,46} and the three different types of GQDs are prepared by controlling the reduction time. The resulting reduced GQDs show enhanced electrical conductivity as the sp^2 carbon bonds are recovered by reduction.^{35,46,48}

The deoxidization of GQDs was investigated by X-ray photoelectron spectroscopy (XPS), Fourier transform infrared spectroscopy (FT-IR) and photoluminescence excitation spectroscopy (PLE). In the C1s X-ray

photoelectron spectra (Figure 2A), the sp^2 carbon peaks at 284.5eV are almost unchanged, while the hydroxyl carbon peaks at 286.0eV and the carbonyl/carboxyl peaks at 287.5~288.7eV decrease with respect to reduction time. We also confirm that the PLE spectrum varies with reduction time as shown in Figure 2B. Usually, GQD exhibits electronic transition processes similar to benzene that shows primary and secondary bands at 202 nm and 255 nm, respectively.⁴⁷ Likewise, GOQD, GQD 5 and GQD 10 show primary excitation bands at ~270 nm and the secondary excitation bands at 310 nm, 315 nm, and 328 nm, respectively. The primary band electronic transition at 270 nm approximately corresponds to the energy gap between π and π^* (~1.55eV), which remains almost constant with increasing reduction time.⁴⁸⁻⁵⁰ This implies that the GQDs are relatively uniform as also shown in the TEM and AFM images (Figure 3 and 6). On the contrary, the secondary bands are remarkably different because the amount of oxygen-related functionality responsible for $n-\pi^*$ transition changes with reduction time.⁵¹⁻⁵³ As a result, the intensity of the secondary excitation band decreases. At the same time, the secondary excitation energy is blue-shifted as the $n-\pi^*$ resonance volume decreases.^{51,52} Thus, we conclude that the reduction is unfavorable for the intensity and range of light absorptivity. However, the increase of sp^2 carbons leads to the better electrical conductivity, which is advantageous for charge carrier transport.

In order to experimentally verify the positive effects of GQDs in BHJ solar cells, GOQD, GQD 5, and GQD 10 were added in the BHJ layer of

PTB7/PC71BM. Figure 3 shows no noticeable size difference between the three different types of GQDs. The GQD content in the BHJ layers was optimized by applying different weight ratios ranging from 0.01 wt% to 0.80 wt% as shown in Figure 7. The optimized ratio was found to be 0.2 wt% for GOQD, 0.5 wt% for GQD 5, and 0.02 wt% for GQD 10, respectively. The device with BHJ layer with GOQDs shows the highest J_{sc} as shown in Figure 4A and Table 1, which is related to the highest IPCE values of the GOQD device in Figure 4B. This confirms that the functional groups on the edge of GOQD play a positive role in light absorption. The UV–visible absorption spectra of GOQDs and its BHJ device showing the higher absorbance than GQDs also support such positive effects (Figure 4C and 8), which is similar to the case of enhanced absorbance by metal nanoparticles.^{23–25} On the other hand, the GQD 5 and GQD10 devices don't exhibit such noticeable light absorption improvement compared to the reference BHJ device.

However, we found that the fill factors are increased from 59.7% to 67.6% for GQD 5 and to 63.5% for GQD 10, respectively. This implies that the reduction of GQDs plays another positive role in carrier conduction. To investigate the contribution of reduced GQDs to FF, we evaluated series resistances (R_s) and shunt resistances (R_{sh}) in J – V measurements. Due to the small changes in resistance factors, the FF value of GOQD device was not much improved compared to the reference (Figure 4D and Table 1). However, the J – V characteristics of partially reduced GQDs (GQD 5) device shows clearly increased R_{sh} and FF as well as decreased R_s . This means that the leakage current can be

slashed by embedding GQD 5. However, the GQD 10 device shows considerably decreased R_{sh} values and power conversion efficiency, which indicates that the reduction level of GQDs needs to be optimized to maximize the performance of the BHJ solar cells.

4. Conclusion

In summary, we have demonstrated that the OPV performance varies with the degree of reduction in GQDs. By controlling the duration of hydrothermal reduction, the strongly oxidized, partially reduced, and strongly reduced GQDs were synthesized. Consequently, we found that the light absorptivity and conductivity of GQDs play different positive roles in enhancing the performance of BHJ OPVs. In case of GOQDs, the presence of functional groups having non-bonding electrons leads to the resonance effect facilitating the secondary excitation at ~ 328 nm. From this property, the device prepared by embedding the GOQDs in BHJ layers showed the considerable enhancement of absorptivity, thereby the increase of J_{sc} . On the other hand, the excitation band varies with reduction time as the functional groups are removed. When the reduced GQDs were embedded in the BHJ layers, the cell performances reach their optimum point even with relatively lower GQD content compared to the GOQD device. This is possibly due to the enhanced metallic property of reduced GQDs. As a result, the adaption of partially reduced GQDs in OPVs improved the FF from 60.4% to 67.6%, thereby enhanced the PCE

from 6.70% to 7.60% by balancing optical absorptivity and electrical conductivity. We believe that this result will provide a new insight to solar cell researchers who want to enhance the efficiency of OPVs by utilizing various quantum dot materials.

5. Reference

1. Sariciftci, N. S.; Smilowitz, L.; Heeger, A. J.; Wudl, F. *Science*, **1992**, *258*, 1474–1476.
2. Yu, G.; Ga, J.; Hummelen, J. C.; Wudl, F.; Heeger, A. J. *Science*, **1995**, *270*, 1789–1791.
3. Heeger, A. J. *Angew. Chem. Int. Ed.* **2001**, *40*, 2591–2611.
4. Park, S. H.; Roy, A.; Beaupr, S.; Cho, S.; Coates, N.; Moon, J. S.; Moses, D.; Leclerc, M.; Lee, K.; Heeger, A. J. *Nat. Photonics* **2009**, *3*, 297–302.
5. Kaltenbrunner, M.; White, M. S.; Głowacki, E. D.; Sekitani, T.; Someya, T.; Sariciftci N. S.; Bauer, S. *Nat. Commun.* **2012**, *3*, 770.
6. Blom, P. W. M.; Mihailetchi, V. D.; Koster, L. J. A.; Markov, D. E. *Adv. Mater.* **2007**, *19*, 1551–1566.
7. Markov, D. E.; Amsterdam, E.; Blom, P. W. M.; Sieval, A. B.; Hummelen, J. C. *J. Phys. Chem. A* **2005**, *109*, 5266–5274.
8. Hau, S. K.; Yip, H. L.; Acton, O.; Baek, N. S.; Ma, H.; Jen, A. K. Y. *J. Mater. Chem.* **2008**, *18*, 5113–5119.

9. Wang, D. H.; Moon, J. S.; Seifert, J.; Jo, J.; Park, J. H.; Park, O. O.; Heeger, A. J. *Nano Lett.* **2011**, *11*, 3163–3168.
10. Hoven, C. V.; Dang, X.-D.; Coffin, R. C.; Peet, J.; Nguyen, T.-Q.; Bazan, G. C. *Adv. Mater.* **2010**, *22*, E63–E66.
11. Ma, W.; Yang, C.; Gong, X.; Lee, K. H.; Heeger, A. J. *Adv. Funct. Mater.* **2005**, *15*, 1617–1622.
12. Brabec, C. J.; Sariciftci, N. S.; Hummelen, J. C. *Adv. Funct. Mater.* **2001**, *11*, 15–26.
13. Huo, L.; Hou, J.; Zhang S.; Chen, H.-Y.; Yang, Y. *Angew. Chem. Int. Ed.* **2010**, *49*, 1500–1503.
14. Sista, S.; Park, M.-H.; Hong, Z.; Wu, Y.; Hou, J.; Kwan, W. L.; Li, G.; Yang, Y. *Adv. Mater.* **2010**, *22*, 380–383.
15. Wang, D. H.; Choi, D. G.; Lee, K. J.; Park, J. H.; Park, O. O. *Langmuir*, **2010**, *26*, 9584–9588.
16. Wang, D. H.; Choi, D. G.; Lee, K. J.; Im, S. H.; Park, O. O.; Park, J. H. *Org. Electron.* **2010**, *11*, 1376–1380.
17. You, J.; Chen, C.-C.; Dou, L.; Murase, S.; Duan, H.-S.; Hawks, S. A.; Xu, T.; Son, H. J.; Yu, L.; Li, G.; Yang, Y. *Adv. Mater.* **2012**, *24*, 5267–5272.
18. Jørgensen, M.; Norrman, K.; Gevorgyan, S. A.; Tromholt, T.; Andreasen, B.; Krebs, F. C. *Adv. Mater.* **2012**, *24*, 580–612.
19. Wang, D. H.; Im, S. H.; Lee, H. K.; Park, O. O.; Park, J. H. *J. Phys. Chem. C* **2009**, *113*, 17268–17273.
20. Atwater, H. A.; Polman, A. *Nat. Mater.* **2010**, *9*, 205–213.
21. Kim, K.; Carroll, D. L. *Appl. Phys. Lett.* **2005**, *87*, 203113.

22. Kim, C.-H.; Cha, S.-H.; Kim, S. C.; Song, M.; Lee, J.; Shin, W.; Moon, S.-J.; Bahng, J. H.; Kotov, N. A.; Jin, S.-H. *ACS Nano*, **2011**, *5*, 3319–3325.
23. Wang, D. H.; Park, K. H.; Seo, J. H.; Seiffter, J.; Jeon, J. H.; Park, J. H.; Park, O. O.; Heeger, A. J. *Adv. Energy Mater.* **2011**, *1*, 766–770.
24. Wang, D. H.; Kim, D. Y.; Choi, K. W.; Seo, J. H.; Im, S. H.; Park, J. H.; Park, O. O.; Heeger, A. J. *Angew. Chem. Int. Ed.* **2011**, *50*, 5519–5523.
25. Wang, D. H.; Kim, J. K.; Lim, G.-H.; Park, K. H.; Park, O. O.; Lim, B.; Park, J. H. *RSC Advances*, **2012**, *2*, 7268–7272.
26. Ren, S.; Chang, L.-Y.; Lim, S.-K.; Zhao, J.; Smith, M.; Zhao, N.; Bulovi, V.; Bawendi, M.; Gradecak, S. *Nano Lett.* **2011**, *11*, 3998–4002.
27. Celik, D.; Krueger, M.; Veit, C.; Schleiermacher, H. F.; Zimmermann, B.; Allard, S.; Dumsch, I.; Scherf, U.; Rauscher, F.; Niyamakom, P.; *Sol. Energy Mater. Sol. Cells* **2012**, *98*, 433–440.
28. Jeltsch, K. F.; Schädel, M.; Bonekamp, J.-B.; Niyamakom, P.; Rauscher, F.; Lademann, H. W. A.; Dumsch, I.; Allard, S.; Scherf, U.; Meerholz, K. *Adv. Funct. Mater.* **2011**, *22*, 397–404.
29. Huynh, W. U.; Dittmer, J. J.; Alivisatos, A. P. *Science* **2002**, *295*, 2425–2427.
30. Jaiswal, J. K.; Goldman, E. R.; Mattoussi, H.; Simon, S. M. *Nat. Methods*, **2004**, *1*, 73–78.
31. Li, Y.; Hu, Y.; Zhao, Y.; Shi, G.; Deng, L.; Hou, Y.; Qu, L. *Adv. Mater.* **2011**, *23*, 776–780.

32. Gupta, V.; Chaudhary, N.; Srivastava, R.; Sharma, G. D.; Bhardwaj, R.; Chand, S. *J. Am. Chem. Soc.* **2011**, *133*, 9960–9963.
33. Shen, J.; Zhu, Y.; Yang, X.; Li, C. *Chem. Commun.* **2012**, *48*, 3686–3699.
34. Wnag, X.; Zhi, L.; Mullen, K. *Nano Lett.* **2007**, *8*, 323–327.
35. Eda, G.; Fanchini, G.; Chhowalla, M. *Nat. Nanotechnol.* **2008**, *3*, 270–274.
36. Robinson, J. T.; Perkins, F. K.; Snow, E. S.; Wei, Z.; Sheehan, P. E. *Nano Lett.* **2008**, *8*, 3137–3140.
37. Robinson, J. T.; Zalalutdinov, M.; Baldwin, J. W.; Snow, E. S.; Wei, Z.; Sheehan, P.; Houston, B. H. *Nano Lett.* **2008**, *8*, 3441–3445.
38. Eda, G.; Lin, Y.-Y.; Miller, S.; Chen, C.-W.; Su, W.-F.; Chhowalla, M. *Appl. Phys. Lett.* **2008**, *92*, 233305.
39. Park, S.; Ruoff, R. S. *Nat. Nanotechnol.* **2009**, *4*, 217–224.
40. Becerill, H. A.; Mao, J.; Liu, Z.; Stoltenberg, R. M.; Bao, Z.; Chen, Y. *ACS Nano* **2008**, *2*, 463–470.
41. Cai, W.; Piner, R. D.; Stadermann, F. J.; Park, S.; Shaibat, M. A.; Ishii, Y.; Yang, D.; Velamakanni, A.; An, S. J.; Stoller, M.; An, J.; Chen, D.; Ruoff, R. S. *Science* **2008**, *321*, 1815–1817.
42. Yang, D.; Velamakanni, A.; Bozoklu, G.; Park, S.; Stoller, M.; Piner, R. D.; Stankovich, S.; Jung, I.; Field, D. A.; Ventrice Jr, C. A.; Ruoff, R. S. *Carbon* **2009**, *47*, 145–152.
43. Li, J.-L.; Kudin, K. N.; McAllister, M. J.; Prud'homme, R. K.; Aksay, I. A.; Car, R. *Phys. Rev. Lett.* **2006**, *96*, 176101.

44. Li, Z.; Zhang, W.; Luo, Y.; Yang, J.; Hou, J. *J. Am. Chem. Soc.* **2009**, *131*, 6320–6321.
45. Pei, S.; Cheng, H.-M. *Carbon* **2012**, *50*, 3210–3228.
46. Zhou, Y.; Bao, Q.; Tang, L. A. L.; Zhong, Y.; Loh, K.P. *Chem. Mater.* **2009**, *21*, 2950–2956.
47. Petruska, J. *J. Chem. Phys.* **1961**, *34*, 1120
48. Eda, G.; Lin, Y.-Y.; Mattevi, C.; Yamaguchi, H.; Chen, H.-A.; Chen, I.-S.; Chen, C.-W.; Chhowalla, M. *Adv. Mater.* **2010**, *22*, 505–509.
49. Liu, H.; Ye, T.; Mao, C. *Angew. Chem. Int. Ed.* **2007**, *46*, 6473–6475.
50. Li, X.; Wang, X.; Zhang, L.; Lee, S.; Dai, H. *Science* **2008**, *319*, 1229–1232.
51. Closson, W.D.; Haug, P. *J. Am. Chem. Soc.* **1964**, *86*, 2384–2389.
52. Sidman, J. W. *Chem. Rev.* **1958**, *58*, 689–713.
53. Luo, Z.; Lu, Y.; Somers, L. A.; Johnson, A. T. C. *J. Am. Chem. Soc.* **2009**, *131*, 898–899.
54. Hirata, M.; Gotou, T.; Horiuchi, S.; Fujiwara, M.; Ohba, M. *Carbon* **2004**, *42*, 2929–2937.
55. Pei, S.; Cheng, H.-M. *Carbon* **2012**, *50*, 3210–3228.
56. Wang, D. H.; Kim, J. K.; Seo, J. H.; Park, I.; Hong, B. H.; Park, J. H.; Heeger, A. J. *Angew. Chem. Int. Ed.* **2013**, *52*, 2874–2880.

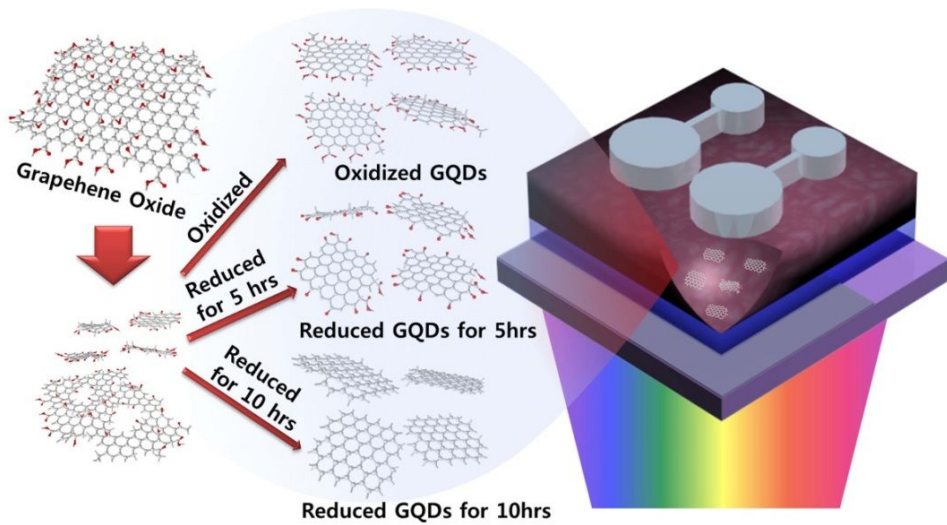


Figure 1. Schematic of BHJ solar cell prepared by addition of three types of GQDs in BHJ layer, of which functional groups on the edge of each GQDs are tuned by reduction times.

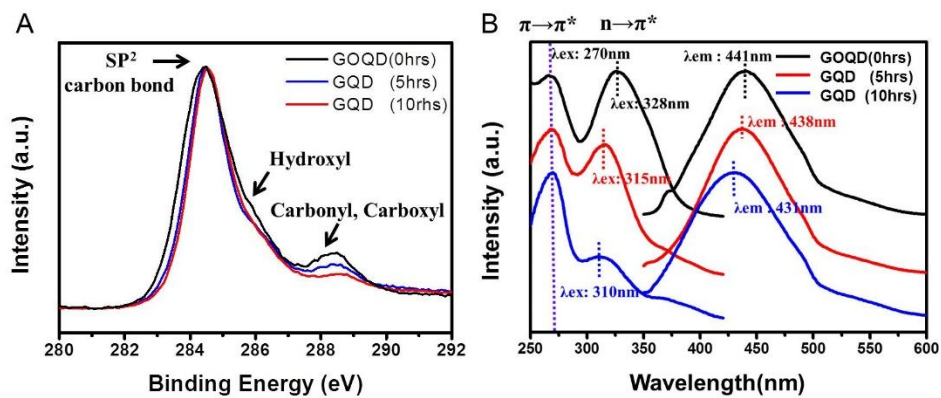


Figure 2. XPS spectra (A) and normalized PLE and PL spectra (B) of GOQD, 5 hrs reduced GQDs, and 10 hrs reduced GQD.

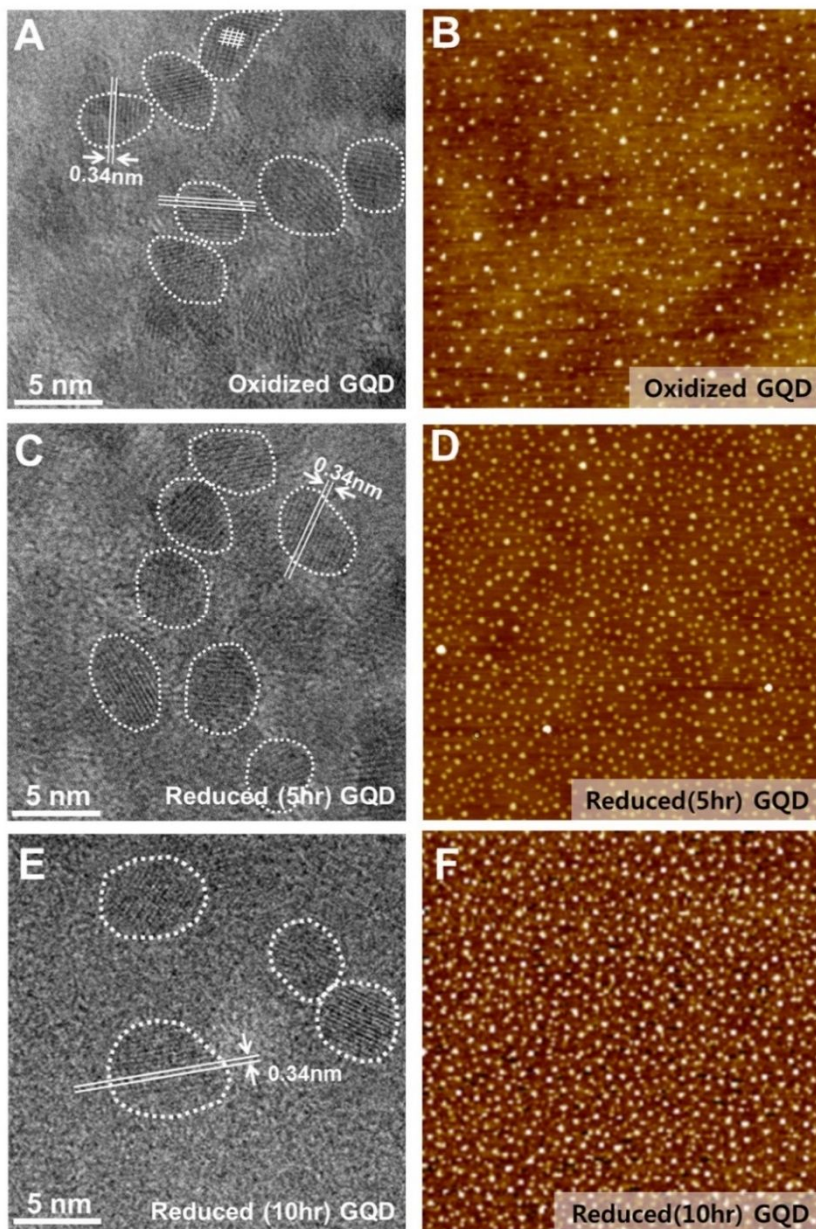


Figure 3. TEM and AFM images of graphene oxide (GO) QDs (A, B), 5 hrs reduced GQDs (C, D), and 10 hrs reduced GQDs (E, F), respectively. The AFM scan ranges are $3 \mu\text{m} \times 3 \mu\text{m}$.

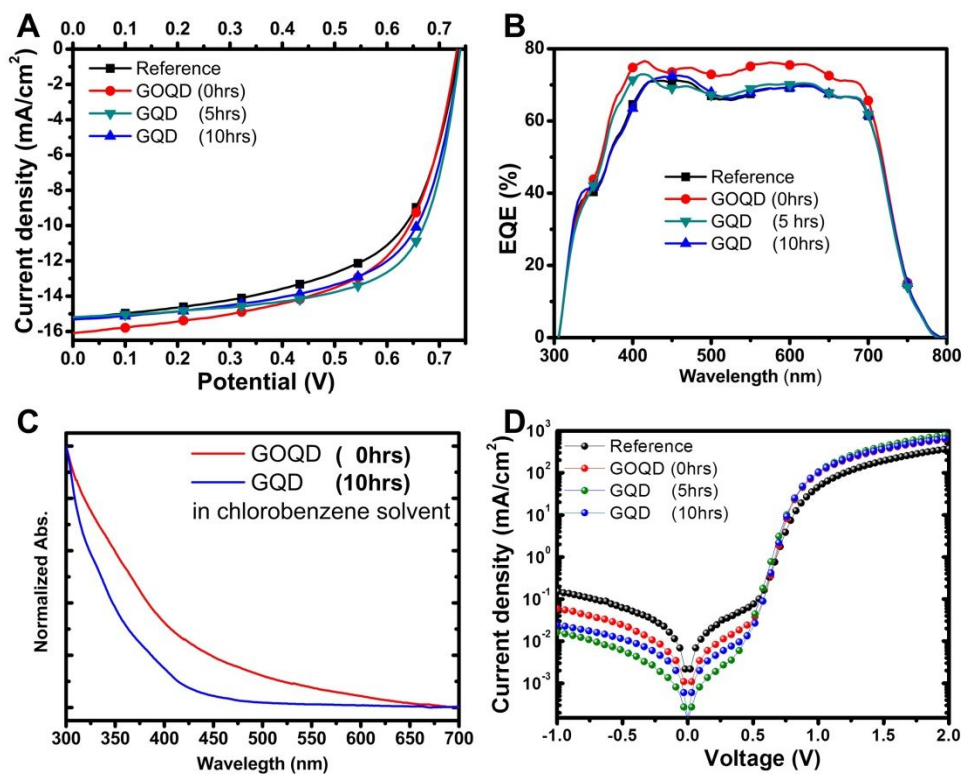


Figure 4. J–V curves (A), IPCE (B) and dark J–V curves (D) of devices with plain BHJ (black), BHJ with GOQD (red), BHJ with GQD 5 (green) or GQD 10 (blue). UV–visible adsorption spectra of GOQD and GQD 10 in chlorobenzene (C).

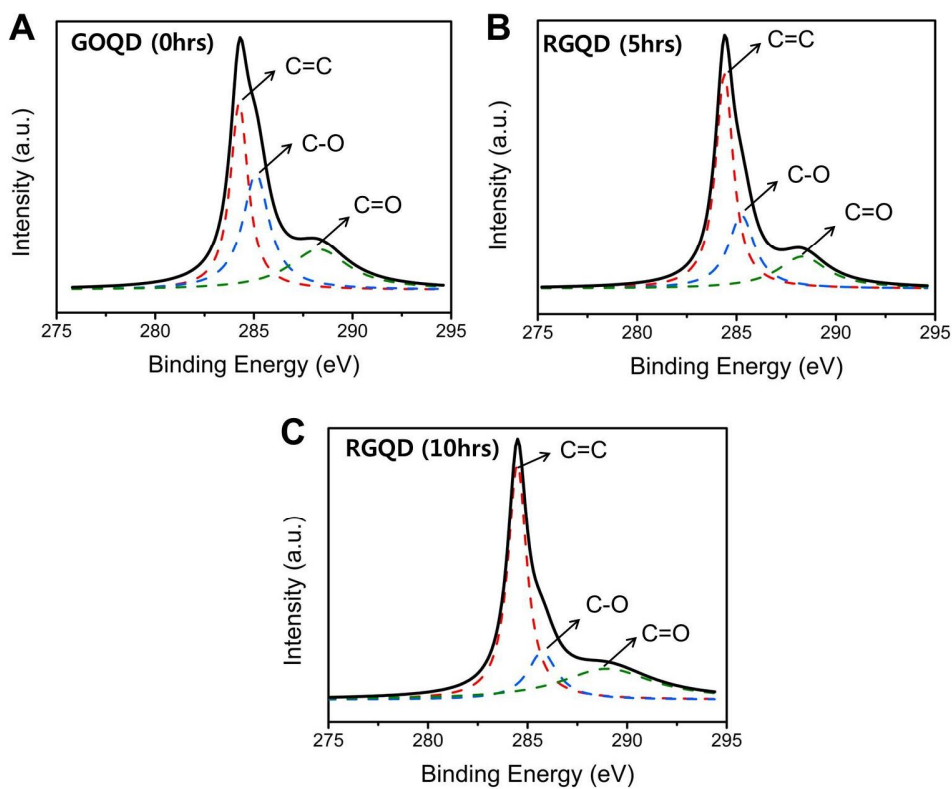


Figure 5. Multi-peaks fitted XPS spectra of GOQD, GQD 5 and GQD 10.

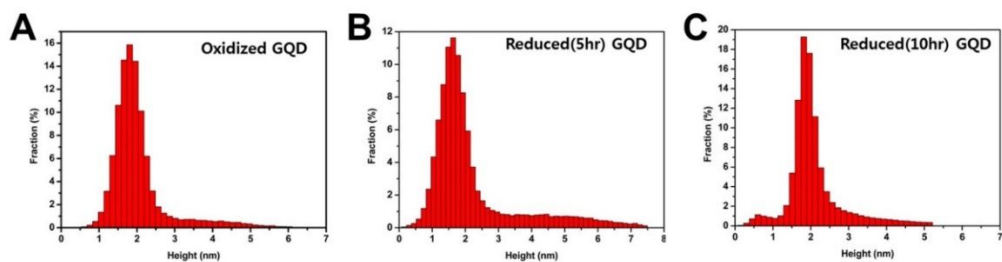


Figure 6. Height distribution (A)~(C) from AFM images in figure 3 of GOQD, GQD 5 and GQD 10.

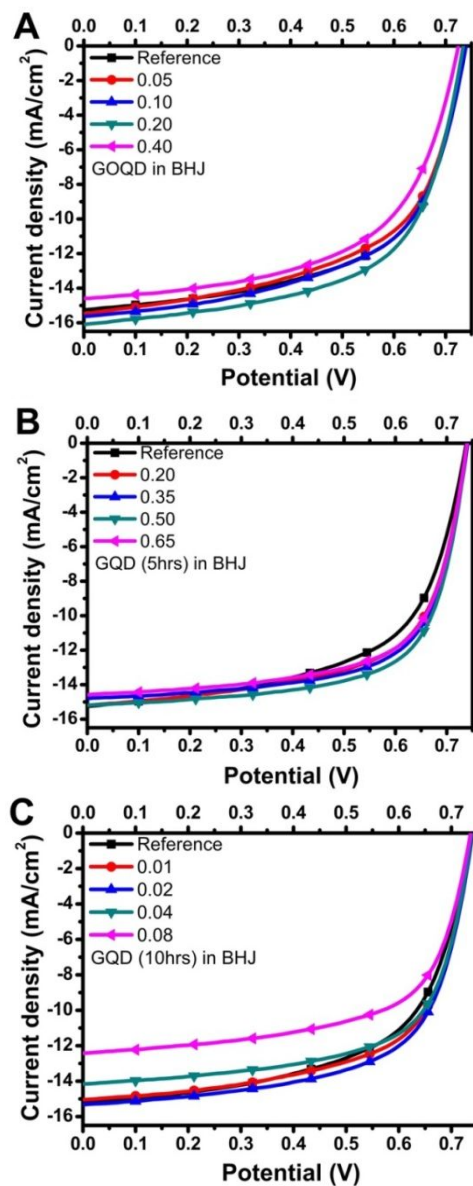


Figure 7. J–V curves of devices prepared by addition of various concentration of GOQD (A), GQD 5 (B) and GQD 10 (C) in BHJ layers.

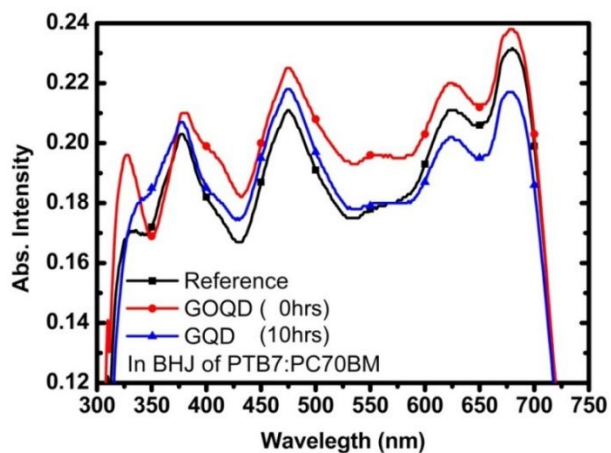


Figure 8. Absorption spectra of plain BHJ film (black) and BHJ films with GOQD (red) and GQD 10 (blue).

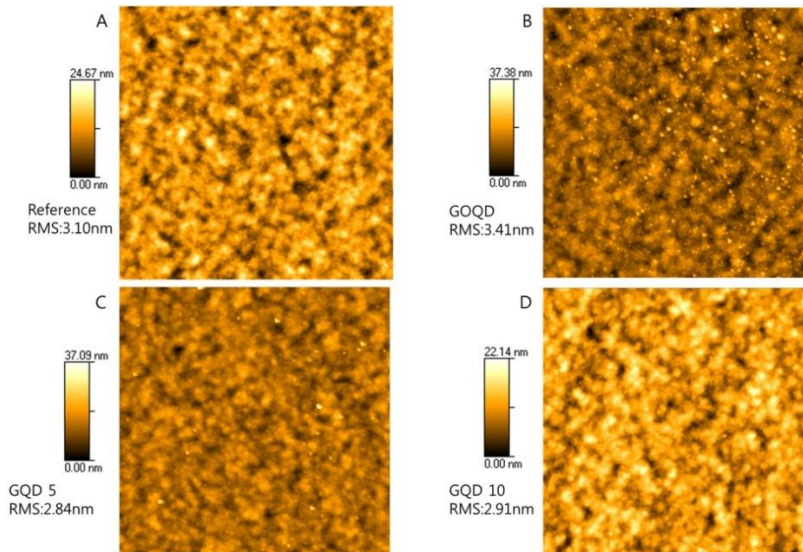


Figure 9. AFM images ($3\ \mu\text{m} \times 3\ \mu\text{m}$) of plain BHJ film (A) and BHJ films with GOQD (B), GQD 5 (C) and GQD 10 (D).

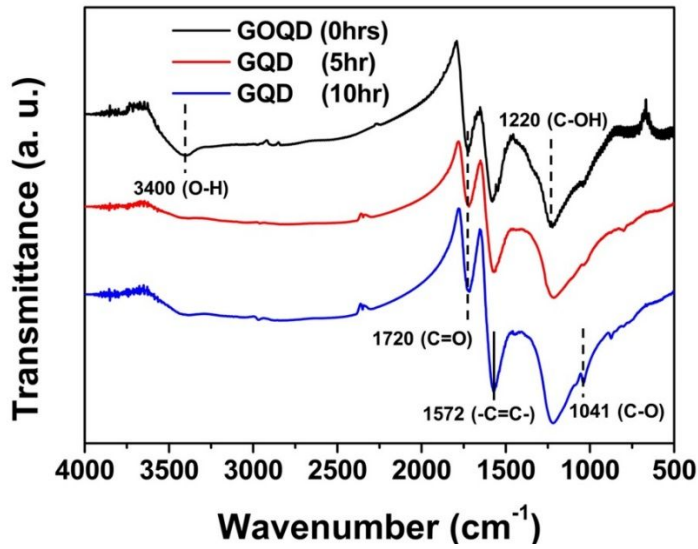


Figure 10. FT-IR spectra of GOQD, GQD 5 and GQD 10.

Device Configuration	PCE (%)	FF (%)	J_{sc} (mA/cm ²)	V_{oc} (V)	R_{Sh} (K Ω cm ²)	R_s (Ω cm ²)
Reference	6.70	59.7	15.2	0.738	8.70	2.87
GOQD (0hrs)	7.11	60.4	16.1	0.733	12.82	2.36
GQD (5hrs)	7.60	67.6	15.2	0.740	26.60	1.80
GQD (10hrs)	7.21	63.6	15.3	0.740	15.20	1.99

Table 1. Performance parameters of the devices with plain BHJ (reference) or BHJ with GOQD, GQD 5 or GQD 10.

Chapter III

Synthesis of Graphene Antidots

1. Introduction

Graphene has been widely studied due to its extraordinary physical properties.^{1,2} When graphene is patterned to have finite nanostructures, this property can be tuned or altered. To prepare such nanostructured graphene, numerous etching methods have been developed.³⁻⁵ Recently, there are interesting reports that this graphene can be also etched by metal nanoparticles (NPs), leading to crystallographic nanopatterns at elevated temperature,^{6,7} which is, however, hardly controllable to form ordered nanostructures on graphene because of migrating NPs. Moreover, a temperature as high as 1000°C for activating metal NPs results in degraded graphene properties. Thus, if NPs are fixed during the catalytic etching of graphene at lower temperature, holes rather than trenches can be formed with minimizing defects induced by the reaction at high temperature. In addition, it does not rely on relatively complicated and time-consuming lithographic processes to create ordered nanostructures on graphene, which enables wafer-scale

fabrication in a time- and cost-effective manner. We believe such less defective graphene nanopores will be very useful for various membrane applications such as DNA sequencing⁸ and ultrafiltration of gas or water molecules⁹.

Here we demonstrate that a regular pattern of nanopores can be fabricated on reduced graphene oxide (rGO) as well as a large-area graphene films synthesized by chemical vapor deposition (CVD), utilizing the catalytic reaction of arrayed Pt NPs synthesized from diblock copolymer micelles. The size and spacing of nanopores can be easily tuned by using various copolymers with different molecular weights. We found that the Pt NPs penetrate the rGO film from top to bottom. On the other hand, the Pt NPs on the CVD graphene do not react with graphene, while the Pt NPs placed under graphene lead to perfect perforation of the graphene films during the annealing at 400 °C in ambient conditions. From systematic AFM and raman analysis, we found that the graphene film transferred on Pt NP arrays is mostly suspended initially, but it is subject to compressive strain during annealing, which provide a good conformal contact with underlying Pt NPs for selective catalytic reaction. As a result, the graphene on the Pt NP arrays undergo substantial mechanical deformation with large strain, which possibly catalyzes the oxidation of sp^2 carbon atoms.

2. Experiment

1. Synthesis of diblock copolymer micelles.

Three polystyrene-*block*-poly(4-vinylpyridine) (PS-P4VP) diblock copolymers (M_n : 32k-13k, PDI = 1.08; M_n : 51k-18k, PDI = 1.15; M_n : 109k-27k, PDI = 1.12) were purchased from Polymer Source Inc. PS-P4VP copolymers were dissolved in toluene to yield a 0.5 wt% micellar solution, which was stirred for 24 h at room temperature and for 3 h at 85 °C and then cooled to room temperature. H_2PtCl_6 , a precursor of Pt NPs, was added to the micellar solution. The molar ratio of precursors to pyridine units in the P4VP block was 0.5 for PS-P4VP (32k-13k) and PS-P4VP (51k-18k), and 0.35 for PS-P4VP (109k-27k). Arrays of Au and SiO_2 NPs were also prepared from PS-P4VP (51k-18k) micelles containing $HAuCl_4$ and tetraethyl orthosilicate with 0.5 molar ratio, respectively.

2. CVD graphene growth and transfer to Pt NPs array.

CVD graphene was synthesized on 25 μ m Cu foil with H_2 and CH_4 flow for 5 and 50sccm respectively at 1000° C for 30mins in a vacuum. After graphene growth, poly(methyl methacrylate) (PMMA) as a supporting layer was coated on one side and the other side was removed by reactive ion etching (RIE). Cu foil can be etched away using ammonium persulfate aqueous solution (20mm), leaving the graphene floating on

solution. The graphene with the supporting layer was rinsed 3 times on distilled water and transferred onto the Pt NPs arrayed substrate. After drying process, the graphene transferred substrate was submerged vertically in acetone for 30min, followed by immersion in isopropanol (IPA) for 2 min. IPA treatment can prevent rupture of graphene surface, which is ascribed to its solubility in acetone, volatilization and lower surface tension than acetone. From these properties, clean surface without crack can be acquired even in natural dry condition.

3. Perforation of rGO and CVD graphene by Pt NPs.

Aqueous GO dispersion (0.1 wt%) was obtained by ultrasonication (2 h) of GO synthesized by the modified Hummers' method, followed by centrifugation at 3000 rpm for 1 h to remove precipitates. The rGO film was prepared by spin coating of GO dispersion five times and followed by hydrazine vapor treatment on a SiO₂(300nm)/Si substrate, which was cleaned in a piranha solution (70/30 v/v concentrated H₂SO₄ and 30% H₂O₂) prior to spin coating. Single layer of PS-P4VP micelles containing precursors of Pt NPs was spin-coated onto an rGO film for 60 s at 4000 rpm for PS-P4VP (32k-13k), and at 2000 rpm for PS-P4VP (51k-18k) and PS-P4VP (109k-27k). To perforate the rGO film by synthesizing Pt NPs with the removal of copolymers, the micellar film on the rGO film was heated at 400 °C for 30 min in air. For the perforated rGO film transfer, the rGO film was spin coated with a PMMA supporting layer and delaminated from the SiO₂/Si substrate by exposing it to an aqueous

NaOH solution (1.0 M). After transfer to another SiO₂/Si substrate, the PMMA layer was removed by mild sonication in acetone. To perforate the CVD graphene, Pt NPs were first synthesized on a SiO₂/Si substrate with the same procedure on an rGO film. The single-layered graphene was then transferred onto the top of Pt NPs using transfer technique as described above. Annealing treatment (400 °C) was exerted to each sample, which was 20mins for PS-P4VP (32k-13k), 30min for PS-P4VP (51k-18k) and 40min for PS-P4VP (109k-27k) respectively. The perforated graphene was transferred to another SiO₂/Si with the same method used for perforated rGO films.

4. Device fabrication.

The SiO₂ (300 nm)/Si²⁺ substrate was used for electrical measurement of perforated graphene field effect transistor. Perforated graphene was spin coated with PMMA and delaminated using aqueous NaOH solution (1.0 M). After several rinsing using distilled water, PMMA coated sample was transferred onto the highly p-doped SiO₂/Si²⁺⁺ substrate and PMMA was removed by acetone. Chromium (5 nm) and gold (30 nm) electrodes were thermally deposited using pre-patterned mask, followed by isolation of graphene channels using photolithography. Each device having different pore size and density was fabricated, forming same channel length (50 μm) and width (200 μm). Drain-source current (I_{ds}) was measured at constant drain-source voltage (V_{ds}) 10mV. Prior to the measurement, all graphene samples

were annealed at 300 °C under H₂/Ar atmosphere.

3. Result and Discussion

We chose different types of graphene, one of which is rGO and the other is CVD graphene. Both materials showed uniformly punched holes with varying pore sizes. Those fabrication mechanisms were extremely different from each other, which is summarized in Figure 1. First, the rGO film was prepared by successive spin-coating of graphene oxide on a SiO₂/Si substrate followed by reduction using hydrazine. The thickness of rGO film is approximately 2.3 nm with uniform surface (rms roughness of 0.4 nm) (Figure 6a). Then, on such rGO film, we spin-coated a single layer polystyrene-*block*-poly(4-vinylpyridine) (PS-P4VP, 51k-18k) micelles with H₂PtCl₆, a precursor of Pt NPs, in the P4VP cores. The AFM image in Figure 2a shows an array of spherical micelles without overlapping, implying a single layer of copolymer micelles. The spacing of micelles obtained by the fast Fourier transformation (FFT) analysis of the image is ~51 nm. Then, we removed the copolymers by heating at 400 °C in air, which resulted in the generation of Pt NPs in the core regions of the micelles as shown in Figure 2b. The heating temperature of 400 °C is known to be safe enough to prevent the degradation of rGO.¹⁰ The spacing of non-aggregated Pt NPs (~51 nm) is identical to that of the original micelles, implying that an array of Pt NPs was successfully fabricated preserving the order of the copolymer micelles.

The height histograms of Pt NPs on rGO before and after annealing indicate that the Pt NPs penetrating the rGO film reside on the SiO₂/Si substrate (Figure 6). To confirm the perforation of rGO, the sample shown in Figure 2b was delaminated and transferred onto another SiO₂/Si substrate for AFM analysis and also on a TEM grid. In the AFM image of the transferred rGO (Figure 2c), we clearly observe arrayed holes with the depth of ~2.2 nm, which is again equivalent to the thickness of rGO (~2.3 nm). These arrayed holes are evidently noticeable in the TEM image (Figure 2d). The spacing of holes (~49 nm in AFM, ~50 nm in TEM) is almost identical to that of Pt NPs (~51 nm), indicating that holes were produced by arrayed Pt NPs. The crystalline structure of Pt NPs was confirmed by the selected-area electron diffraction pattern (Inset of Figure 7b).

When Pt NPs were synthesized on rGO, they directly contacted the rGO surface at the beginning. Since rGO has many oxygen-containing defective sites on its surface, catalytic oxidation of rGO by Pt NPs could be initiated from these surface defects and facilitated by oxygen molecules in air, resulting in the formation of holes in rGO by eliminating carbon atoms near Pt NPs. Once Pt NPs touched the substrate by etching the rGO around Pt NPs, no further oxidation by catalytic Pt NPs could proceed in lateral directions. Pt NPs were immobile when they were synthesized on a bare SiO₂/Si substrate at 400 °C. Thus, Pt NPs perforated rGO from the top of rGO. Since the size of holes (~15 nm) is somewhat larger than the diameter of NPs (~10 nm), there would be a small positional drift or deformation of NPs (Figure 7b).

One of the merits of the diblock copolymer micellar approach is the controllability of the size and spacing of NPs. We employed a lower molecular weight copolymer PS-P4VP (32k-13k) and also a higher one PS-P4VP (109k-27k) than previously utilized PS-P4VP (51k-18k). We repeated the same procedure as before to generate nanoholes in rGO. Since the length of the PS corona block eventually governs the spacing of nanoholes, we obtained a smaller spacing of holes (~34 nm) with PS-P4VP (32k-13k), *i.e.* dense holes, and a larger one (~101 nm) with PS-P4VP (109k-27k), *i.e.* sparse holes, as shown in AFM and TEM images (Figure 8). These spacing values are consistent with those of Pt NPs (Figure 7). For the size of holes, which depends on the length of the P4VP core block, smaller holes (~8 nm) and larger holes (~19 nm) were produced by PS-P4VP (32k-13k) and PS-P4VP (109k-27k), respectively. Overall, we were able to generate the arrays of discrete nanoholes in rGO with controllable sizes and spacing by regulating the molecular weights of copolymers.

Next, we applied the diblock copolymer micellar approach to perforate CVD graphene. We simply followed the same procedure as the previous rGO perforation, but the aggregations of Pt NPs were observed on the CVD graphene (Figure 9). Considering the similar phenomenon observed on graphite surface, the aggregation of Pt NPs might be due to the low surface energy of graphene¹¹ and low temperature (400 °C) that cannot activate thermal decomposition of sp² carbon-carbon bonds. Thus, previous methods usually employed the temperature higher than 1,000 °C to promote the reaction, which is unfavorable for maintaining the high

quality graphene. In this regard, a catalytic condition that can lower the reaction energy barrier is desirable, which includes the use of catalysts or strain-induced sp^2 - sp^3 bond character changes.¹²⁻¹⁵ In particular, the Pt NPs lying under graphene is useful to generate highly localized strain that can alter the bond characteristics of graphene, leading to efficient perforation at lower temperature.

We first synthesized arrayed Pt NPs from PS-P4VP (51k-18k) on a bare SiO_2/Si substrate and transferred CVD graphene on top (Figure 2e and 2f). The transferred graphene on the Pt NPs tends to be suspended across a few Pt NPs (Figure 2f). At the initial stage of the annealing process (Figure 10b to 10d), the graphene seems to experience the local strain increasing with time due to the difference in thermal expansion coefficient between graphene and Pt NPs.¹⁶⁻¹⁹ The suspended regions disappear after 30 min (Figure 2g) as the Pt NPs perforate the graphene from bottom to top, which is clearly shown in the 3D views of the AFM images before and after heating (Figure 2f and 2g). To confirm the perforation in CVD graphene, the sample shown in Figure 2g was delaminated and transferred onto another SiO_2/Si substrate. In the AFM image of the transferred graphene (Figure 2h), we can clearly observe the arrayed holes. The spacing of the holes (~ 56 nm) is close to that of the Pt NPs (~ 51 nm). The hole array can be also observed in the TEM image of the perforated graphene (Figure 11).

We further explored the mechanism of the perforation in CVD graphene with varying annealing time using Raman spectroscopy. Dozens of random points of each sample were measured and classified to

elucidate the correlation between strain and doping effects. The Raman G and 2D bands for graphene transferred on Pt NPs before annealing were observed at $1580.4 \pm 1.7 \text{ cm}^{-1}$ and $2671.9 \pm 3.7 \text{ cm}^{-1}$ and shifted to $1597.4 \pm 1.0 \text{ cm}^{-1}$ and $2691.4 \pm 1.4 \text{ cm}^{-1}$ after 30 min, respectively (Figure 3a). This indicates that the annealing generally induces strong p-doping effect,²⁰ but the large downshift of G peak at 1577.1 cm^{-1} from the suspended region cannot be explained only by doping effect,²¹ and is possibly correlated with mechanical strain²²⁻²⁴ between the graphene and its underlying substrate.²⁵ From these, we assume that both mechanical deformation and the doping of graphene are critical factors that promote the catalytic perforation of graphene by Pt NPs during annealing process.

The 2D/G ratio is a typical means to estimate the doping concentration. The double resonant process (2D peak) in the inter-valley is strongly affected by doping effect, which induces decreasing intensity owing to electron-electron scattering effect.²⁶ The 2D/G ratio gradually decreases and the frequency of G band increases with annealing time and saturates after 30 min (Figure 3b). This implies that the graphene on Pt NPs is influenced by the thermally induced p-doping effect.

The G band broadening (Figure 3c) appearing at 5 to 20 minutes support the dominance of mechanical strain²³⁻²⁵ rather than doping effect that leads to the sharpening of the G band.²⁷ After annealing for 30 min, the Raman data points look similar to those before annealing. This exhibits that the strain is released as the graphene is perforated by Pt

NPs, where the local curvatures provide the sp^3 -like reactive sites for adsorbed molecules such as oxygen.²⁰⁻²³ Finally, the oxidized carbons decompose into CO or CO₂, resulting in the nanohole arrays of graphene as shown in Figure 2h. The 2D band broadening (Figure 12) also manifests the role of mechanical strain in the perforation of graphene by Pt NPs.²⁴

Recently, Lee *et al.* reported Raman studies on the optical separation of mechanical strain from doping in graphene,²⁵ where e_H , ε_C , and ε_T vectors represent doping concentration, compressive strain, and tensile strain, respectively (Inset of Figure 3d). As shown in Fig. 3D, we borrowed this concept to elucidate the detailed mechanism of perforation by Pt NPs, which indicates that the strained graphene by Pt NPs follows the uniaxial slope ($\Delta\omega_{2D}/\Delta\omega_G = 2.2 \pm 0.2$) as well as the hole doping slope (0.75 ± 0.04) with annealing time.

The graphene on SiO₂ substrates typically shows the p-doping of $\sim 3.55 \times 10^{12} \text{ cm}^{-2}$ and the compressive strain (ε_C) of $\sim 0.15\%$ that is caused by slippage and shrinkage during the drying process at $\sim 80^\circ \text{ C}$ (gray dots in Figure 3d).¹³ On the other hand, the graphene on NPs arrays remarkably experiences the tensile strain (ε_T) of $\sim 0.16\%$ (point A in Figure 3d), resulting in the downshift of G peaks at $\sim 1577.1 \text{ cm}^{-1}$ (blue dots in Figure 3d). The hole doping level is $\sim 3.8 \times 10^{12} \text{ cm}^{-2}$ (point B in Figure 3d), which is similar to the graphene on SiO₂. The shift of data points after transfer onto Pt NP arrays looks parallel to the uniaxial slope in general, but rather wide distributions and relatively steeper slopes imply the coexistence of suspended regions that leads to

the biaxial buckling graphene as shown in Figure 2f.²⁸⁻³⁰ After 10 min annealing, the distribution mostly changes back to confined quasi linearity and follows the uniaxial type (purple dots in Figure 3d). This spectral change indicates that the negative thermal expansion of graphene tends to form uniaxial strain along the linear wrinkles bridged by adjacent Pt NPs rather than biaxial strain as shown in Figure 2g. In addition, the region of distribution is upshifted with a slightly declined slope, suggesting that the graphene was p-doped. The appearance of the hole doping ($6.0 \times 10^{12} \text{ cm}^{-2}$) is possibly caused by the attachment of oxygen molecules on the graphene surface.¹³ After 20 min annealing, the degree of distribution is more perturbed and the slope is declined towards the hole doping slope. We suppose that the spectral inhomogeneity after 20 min annealing is originated from the increased hole doping by oxidation reaction at structurally deformed sites (pink dots in Figure 3d). The continuing annealing up to 30 min further p-dopes the deformed graphene on Pt NP arrays, and finally, the compressive strain is released as the graphene is perforated by the Pt NP-assisted oxidation reaction (See red dots with no linearity assigned to strain in Figure 3d). After complete perforation, the final compressive strain is appeared to be $\sim 0.22 \%$ at a p-doping level of $\sim 1.2 \times 10^{13} \text{ cm}^{-2}$ (Table 1). The gradual appearance of defect-related D and D' peaks as well as the shift of G and 2D peaks also support that the perforation proceeds with increasing annealing time (Figure 13). Thus, we conclude that the localized strain and the oxidation reaction by Pt NPs cooperatively contribute the strain-assisted perforation of graphene.

As previously shown in rGO case, the size and spacing of the nanopore arrays on the CVD graphene can be also tuned by regulating the molecular weight of copolymers (number of pores per unit area, $\sim 1.0 \times 10^{10} \text{ cm}^{-2}$, $\sim 3.4 \times 10^{10} \text{ cm}^{-2}$, and $\sim 6.0 \times 10^{10} \text{ cm}^{-2}$, for Figure 4a to 4c, respectively). This observation is consistent with Raman spectra, in which the intensity of D peak appears to be proportional to nanopore density (Figure 4d).

To investigate the electrical properties of the perforated graphene, we fabricated the field effect transistor (FET) (Figure 4e). We calculated the charge neutral point of nanoporated graphene shown in Figure 4b from its p-doping concentration ($1.2 \times 10^{13} \text{ cm}^{-2}$) to be $\sim 167 \text{ V}$,³³ which is beyond the upper limit of our measurement set-up. Thus, we carried out the H_2/Ar annealing treatment at $300 \text{ }^\circ\text{C}$ for 10 min prior to the measurement to reduce the doping level, allowing us to observe the charge neutral points of FETs (solid lines in Figure 4e). The charge neutral points shift more dramatically when H_2/Ar annealing process takes longer (dashed lines in Figure 4e and Figure 14). The different charge neutral points of perforated graphene FETs show that the Fermi level is closely related to the nanopore density. Note that $I_{\text{ds}}-V_{\text{g}}$ curves are asymmetric because of a difference in the conductance of holes and electrons.³⁴ Electrical properties seems to act as a p-type graphene based FET rather than semiconductor, which may be attributed to relatively large spacing among holes against previous report.⁵ We think that the neck width of perforated graphene should be scaled down below 20 nm to have semiconducting properties, which will be further studied

in our following researches. As opposed to doping correlation, current level is inversely proportional to high pore density, which once again demonstrate the rate of carbon decomposition at each sample.

We have performed several control experiments to confirm the catalytic role of Pt NPs. First, graphene on a bare substrate heated at 400 °C in air showed no changes regardless of annealing time. Second, graphene on Pt NP arrays heated at 400 °C in vacuum resulted in formation of many ripples but no perforation (Figure 5a), implying that oxygen molecules are essential for perforation in addition to structural deformation. Third, instead of Pt NPs, graphene was transferred on SiO₂ NP and Au NP arrays, and then heated at 400 °C in air, but no signature of perforation was observed both in AFM images (Figure 5b and 5c) and Raman spectra (Figure 5d), suggesting that Pt plays an important role as a catalyst to perforate graphene. We suppose that the use of Pt NPs as catalysts lowers the activation energy needed for perforation reaction, while the non-catalytic SiO₂ NPs requires more thermal activation energy and reaction temperature as high as 1,100 °C.³¹

4. Conclusion

We successfully fabricated rGO and CVD graphene films patterned with nanopore arrays using Pt NP arrays whose sizes and spacing are controllable by using different diblock copolymer precursors. We confirmed that the perforation reaction is catalyzed by Pt NPs lowering the activation energy barriers for the oxidation reaction of carbon atoms, where the mechanical strain should be additionally considered for the perforation of CVD graphene. The method of using diblock copolymers is scalable above a wafer scale (Figure 15), and thus, it is expected to provide a practical route to fabricate large-area nanopatterned graphene without employing complicated lithography processes. The suggested perforation mechanism by Pt NPs can be compared with using different metals such as Ag, Ni, and Fe utilized for randomly directional patterning at high temperature,^{6,7,32} which are unlike the case of using diblock copolymer method. In addition, the further studies on the chemistry and strain-engineering between

graphene and metal catalysts would be useful to understand the properties of graphene, which utilized for various electronic, chemical, biological, and environmental applications.

5. Reference

1. Geim, A. K.; Novoselov, K. S. The Rise of Graphene. *Nat. Mater.* **2007**, *6*, 183–191.
2. Lee, C.; Wei, X.; Kysar, J. W.; Hone, J. Measurement of the Elastic Properties and Intrinsic Strength of Monolayer Graphene. *Science* **2008**, *321*, 385–388.
3. Ruiz, R.; Kang, H.; Detcheverry, F. A.; Dobisz, E.; Kercher, D. S.; Albrecht, T. R.; de Pablo, J. J.; Nealey, P. F. Density Multiplication and Improved Lithography by Directed Block Copolymer Assembly. *Science* **2008**, *321*, 936–939.
4. Zeng, Z.; Huang, X.; Yin, Z.; Li, H.; Chen, Y.; Li, H.; Zhang, Q.; Ma, J.; Boey, F.; Zhang, H. Fabrication of Graphene Nanomesh by Using an Anodic Aluminum Oxide Membrane as a Template. *Adv. Mater.* **2012**, *24*, 4138–4142.
5. Bai, J.; Zhong, X.; Jiang, S.; Huang, Y.; Duan, X. Graphene Nanomesh. *Nat. Nanotechnol.* **2010**, *5*, 190–194.
6. Datta, S. S.; Strachan, D. R.; Khamis, S. M.; Johnson, A. T. C.

- Crystallographic Etching of Few-Layer Graphene. *Nano Lett.* **2008**, *8*, 1912–1915.
7. Severin, N.; Kirstein, S.; Sokolov, I. M.; Rabe, J. P. Rapid Trench Channeling of Graphenes with Catalytic Silver Nanoparticles. *Nano Lett.* **2009**, *9*, 457–461.
 8. Schneider, G. F.; Kowalczyk, S. W.; Calado, V. E.; Pandraud, G.; Zandbergen, H. W.; Vandersypen, L. M. K.; Dekker, C. DNA Translocation through Graphene Nanopores. *Nano Lett.* **2010**, *10*, 3163–3167.
 9. Celebi, K.; Buchheim, J.; Wyss, R. M.; Droudian, A.; Gasser, P.; Shorubalko, I.; Kye, J.-I.; Lee, C.; Park, H. G. Ultimate Permeation Across Atomically Thin Porous Graphene. *Science* **2014**, *344*, 289–292.
 10. Stankovich, S.; Dikin, D. A.; Piner, R. D.; Kohlhaas, K. A.; Kleinhammes, A.; Jia, Y.; Wu, Y.; Nguyen, S. T.; Ruoff, R. S. Synthesis of Graphene-Based Nanosheets via Chemical Reduction of Exfoliated Graphite Oxide. *Carbon* **2007**, *45*, 1558–1565.
 11. Bardotti, L.; Jensen, P.; Hoareau, A.; Treilleux, M.; Cabaud, B.; Perez, A.; Aires, F. C. S. Diffusion and Aggregation of Large Antimony and Gold Clusters Deposited on Graphite. *Surf. Sci.* **1996**, *367*, 276–292.
 12. Haddon, R. C. Chemistry of the Fullerenes: The Manifestation of Strain in a Class of Continuous Aromatic Molecules. *Science* **1993**, *261*, 1545–1550.
 13. Ryu, S.; Liu, L.; Berciaud, S.; Yu, Y.-J.; Liu, H.; Kim, P.; Flynn, G. W.; Brus, L. E. Atmospheric Oxygen Binding and Hole Doping in

- Deformed Graphene on a SiO₂ Substrate. *Nano Lett.* **2010**, *10*, 4944–4951.
14. Bissett, M. A.; Konabe, S.; Okada, S.; Tsuji, M.; Ago, H. Enhanced Chemical Reactivity of Graphene Induced by Mechanical Strain. *ACS Nano* **2013**, *7*, 10335–10343.
 15. Wu, Q.; Wu, Y.; Hao, Y.; Geng, J.; Charlton, M.; Chen, S.; Ren, Y.; Ji, H.; Li, H.; Boukhvalov, D. W.; Piner, R. D.; Bielawski, C. W.; Ruoff, R. S. Selective Surface Functionalization at Regions of High Local Curvature in Graphene. *Chem. Commun.* **2013**, *49*, 677–679.
 16. Levy, N.; Burke, S. A.; Meaker, K. L.; Panlasigui, M.; Zettl, A.; Guinea, F.; Neto, A. H. C.; Crommie, M. F. Strain-Induced Pseudo-Magnetic Fields Greater than 300 Tesla in Graphene Nanobubbles. *Science* **2010**, *329*, 544–547.
 17. Bao, W.; Miao, F.; Chen, Z.; Zhang, H.; Jang, W.; Dames, C.; Lau, C. N. Controlled Ripple Texturing of Suspended Graphene and Ultrathin Graphite Membranes. *Nat. Nanotechnol.* **2009**, *4*, 562–566.
 18. Chen, C.-C.; Bao, W.; Theiss, J.; Dames, C.; Lau, C. N.; Cronin, S. B. Raman Spectroscopy of Ripple Formation in Suspended Graphene. *Nano Lett.* **2009**, *9*, 4172–4176.
 19. Yoon, D.; Son, Y.-W.; Cheong, H. Negative Thermal Expansion Coefficient of Graphene Measured by Raman Spectroscopy. *Nano Lett.* **2011**, *11*, 3227–3231.
 20. Liu, L.; Ryu, S.; Tomasik, M. R.; Stolyarova, E.; Jung, N.; Hybertsen, M. S.; Steigerwald, M. L.; Brus, L. E.; Flynn, G. W. Graphene Oxidation: Thickness-Dependent Etching and Strong Chemical

- Doping. *Nano Lett.* **2008**, *8*, 1965–1970.
21. Berciaud, S.; Ryu, S.; Brus, L. E.; Heinz, T. F. Probing the Intrinsic Properties of Exfoliated Graphene: Raman Spectroscopy of Free–Standing Monolayers. *Nano Lett.* **2009**, *9*, 346–352.
 22. Mohiuddin, T. M. G.; Lombardo, A.; Nair, R. R.; Bonetti, A.; Savini, G.; Jalil, R.; Bonini, N.; Basko, D. M.; Galiotis, C.; Marzari, N.; Novoselov, K. S.; Geim, A. K.; Ferrari, A. C. Uniaxial strain in graphene by Raman spectroscopy: G peak splitting, Grüneisen parameters, and sample orientation. *Phys. Rev. B* **2009**, *79*, 205433.
 23. Huang, M.; Yan, H.; Chen, C.; Song, D.; Heinz, T. F.; Hone, J. Phonon Softening and Crystallographic Orientation of Strained Graphene Studied by Raman Spectroscopy. *Proc. Natl. Acad. Sci. U.S.A.* **2009**, *106*, 7304–7308.
 24. Frank, O.; Tsoukleri, G.; Parthenios, J.; Papagelis, K.; Riaz, I.; Jalil, R.; Novoselov, K. S.; Galiotis, C. Compression Behavior of Single–Layer Graphenes. *ACS Nano* **2010**, *4* (6), 3131–3138.
 25. Lee, J. E.; Ahn, G.; Shim, J.; Lee, Y. S.; Ryu, S. Optical Separation of Mechanical Strain from Charge Doping in Graphene. *Nat. Commun.* **2012**, *3*, 1024.
 26. Basko, D. M.; Piscanec, S.; Ferrari, A. C., Electron–Electron Interactions and Doping Dependence of the Two–Phonon Raman Intensity in Graphene. *Phys. Rev. B* **2009**, *80*, 165413.
 27. Das, A.; Pisana, S.; Chakraborty, B.; Piscanec, S.; Saha, S. K.; Waghmare, U. V.; Novoselov, K. S.; Krishnamurthy, H. R.; Geim, A. K.; Ferrari, A. C.; Sood, A. K. Monitoring Dopants by Raman

- Scattering in an Electrochemically Top-Gated Graphene Transistor. *Nat. Nanotechnol.* **2008**, *3*, 210–215.
28. Metzger, C.; Rémi, S.; Liu, M.; Kusminskiy, S. V.; Castro Neto, A. H.; Swan, A. K.; Goldberg, B. B. Biaxial Strain in Graphene Adhered to Shallow Depressions. *Nano Lett.* **2010**, *10*, 6–10.
29. Ding, F.; Ji, H.; Chen, Y.; Herklotz, A.; Dörr, K.; Mei, Y.; Rastelli, A.; Schmidt, O. G. Stretchable Graphene: A Close Look at Fundamental Parameters through Biaxial Straining. *Nano Lett.* **2010**, *10*, 3453–3458.
30. Zabel, J.; Nair, R. R.; Ott, A.; Georgiou, T.; Geim, A. K.; Novoselov, K. S.; Casiraghi, C. Raman Spectroscopy of Graphene and Bilayer under Biaxial Strain: Bubbles and Balloons. *Nano Lett.* **2012**, *12*, 617–621.
31. Gao, L.; Ren, W.; Liu, B.; Wu, Z.-S.; Jiang, C.; Cheng, H.-M., Crystallographic Tailoring of Graphene by Nonmetal SiO_x Nanoparticles. *J. Am. Chem. Soc.* **2009**, *131*, 13934–13936.
32. Campos, L. C.; Manfrinato, V. R.; Sanchez-Yamagishi, J. D.; Kong, J.; Jarillo-Herrero, P., Anisotropic Etching and Nanoribbon Formation in Single-Layer Graphene. *Nano Lett.* **2009**, *9*, 2600–2604.
33. Novoselov, K. S.; Geim, A. K.; Morozov, S. V.; Jiang, D.; Zhang, Y.; Dubonos, S. V.; Grigorieva, I. V.; Firsov, A. A. Electric Field Effect in Atomically Thin Carbon Films. *Science* **2004**, *306*, 666–669.
34. Farmer, D. B.; Golizadeh-Mojarad, R.; Perebeinos, V.; Lin, Y.-M.; Tulevski, G. S.; Tsang, J. C.; Avouris, P., Chemical Doping and Electron-Hole Conduction Asymmetry in Graphene Devices. *Nano Lett.* **2009**, *9*, 388–392.

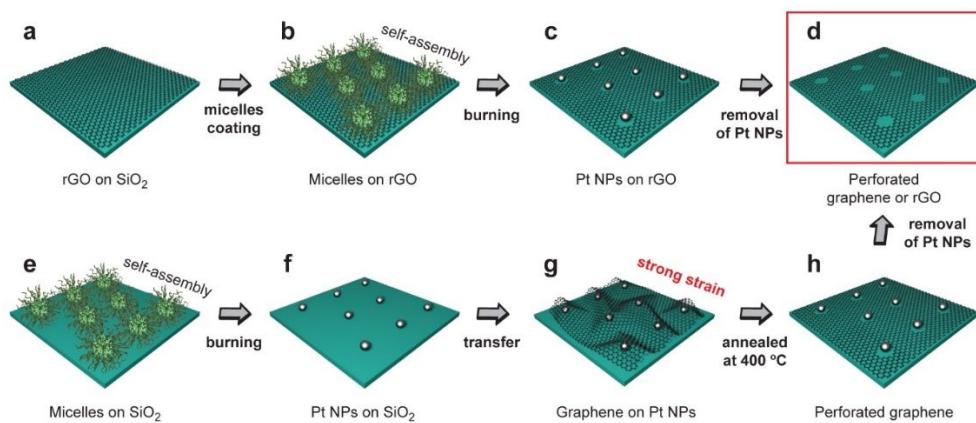


Figure 1. Schematic of fabrication of nanoscale perforated graphene films. (a) Reduced graphene oxide (rGO) is coated on a SiO_2/Si substrate. (b) Diblock copolymer micelles incorporated with Pt precursors is coated on the rGO film. (c) The Pt NPs array is formed with penetration from top of rGO at 400°C in ambient condition. (d) The nanopores are formed on rGO or CVD graphene. (e) Diblock copolymer micelles incorporating with

Pt precursors are first coated on the SiO₂/Si substrate. (f) The micelles film is converted into Pt NPs array after annealing at 400°C in ambient condition. (g) The CVD graphene is transferred on the Pt NPs array, followed by annealing at 400 °C. (h) Local strain on graphene induced by negative thermal expansion leads to enhanced chemical reactivity resulting in localized catalytic perforation.

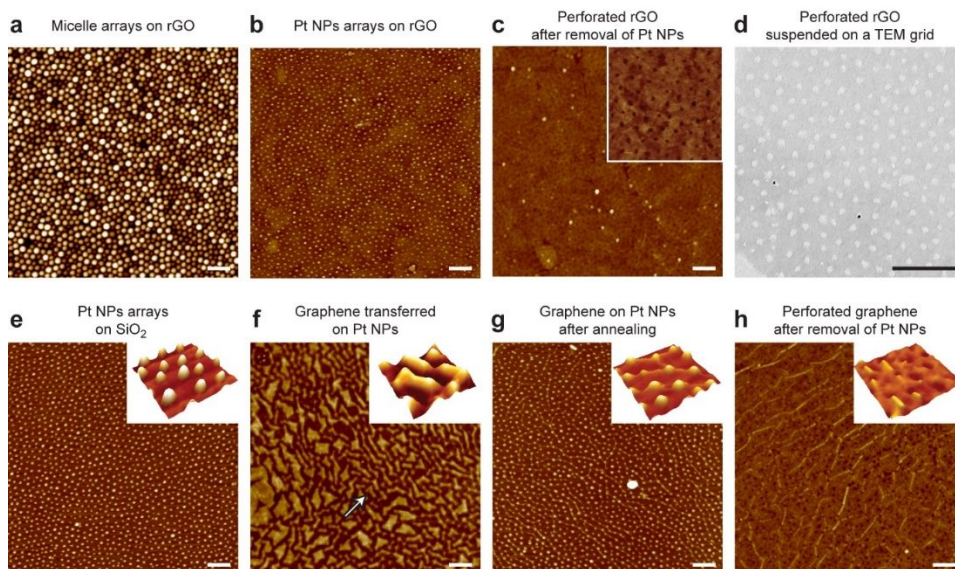


Figure 2. AFM and TEM images for perforation processes. (a) AFM image of uniformly coated Pt–micelle arrays on rGO. (b) AFM image of well arrayed Pt NPs, on rGO after annealing. (c) AFM image of perforated rGO after transfer to another substrate. (d) TEM image of nanopores of rGO suspended in a TEM grid. (e) AFM image of the Pt

NPs array on a SiO₂/Si substrate after annealing. (f) AFM image of CVD graphene transferred on the Pt NPs array. (g) AFM image of CVD graphene subjected to local strain caused by annealing treatment. (h) AFM image of nanopores formed on CVD graphene after removing Pt NPs. Scale bars in AFM and TEM images are 200 nm.

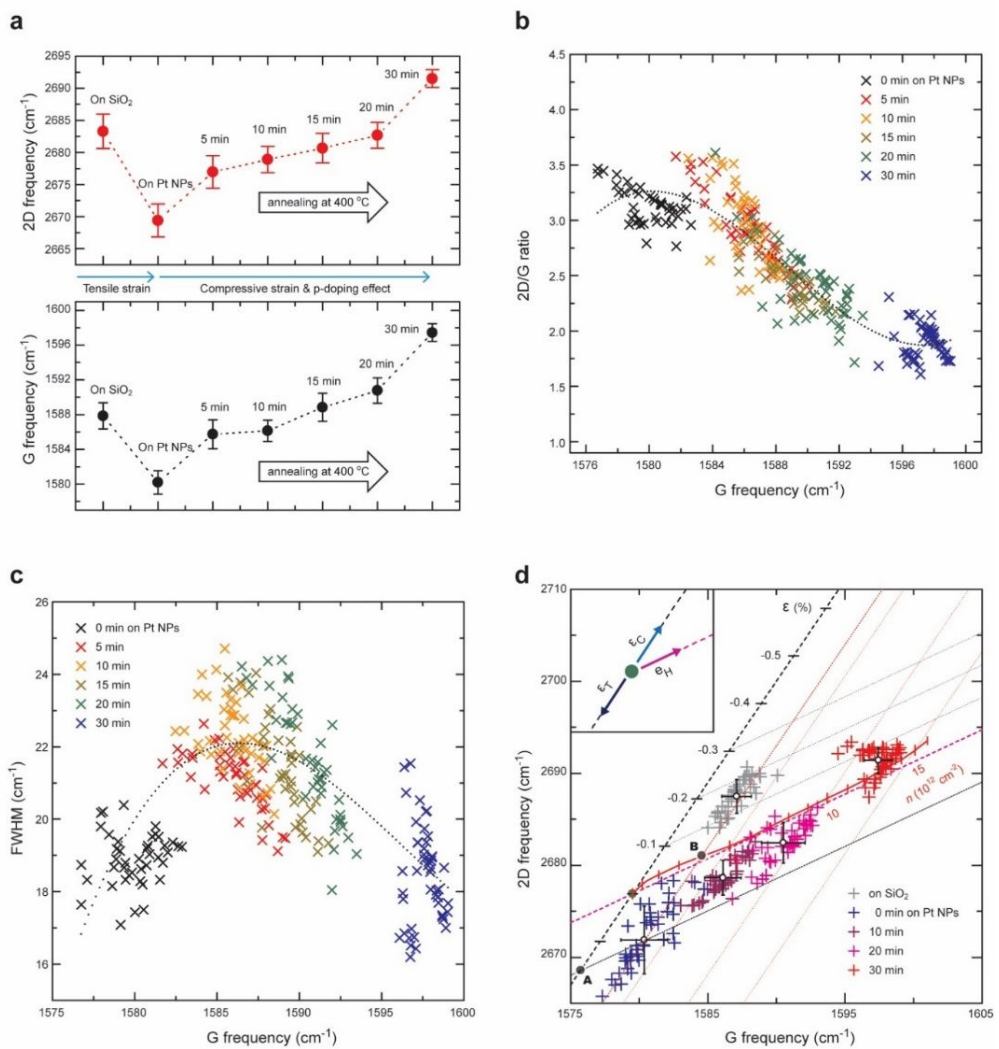


Figure 3. Raman analyses of CVD graphene on Pt NPs with respect to

annealing time. (a) The variation of the phonon frequencies of the 2D and G modes as a function of annealing time. (b) Correlation between 2D/G intensity ratio and G mode position as a function of each annealing treated samples (Black dashed line represents second order polynomial curve fit to the data points). (c) Correlation between FWHM of G mode and its position as a function of each annealing treated samples (Black dashed line represents second order polynomial curve fit to the data points). (d) Correlation between the G and 2D modes varied by annealing. The black dashed line indicates the charge neutral graphene under randomly oriented uniaxial strain. The red solid line indicates doped graphene with varying density of holes, Green dot indicates the charge neutral and strain-free graphene. (Inset: decomposition of hole doping and strain types using unit vectors; ϵ_C : compressive strain, ϵ_T : tensile strain, e_H : hole doping effect, magenta dashed line: average value of strain-free graphene with varying density of holes.)

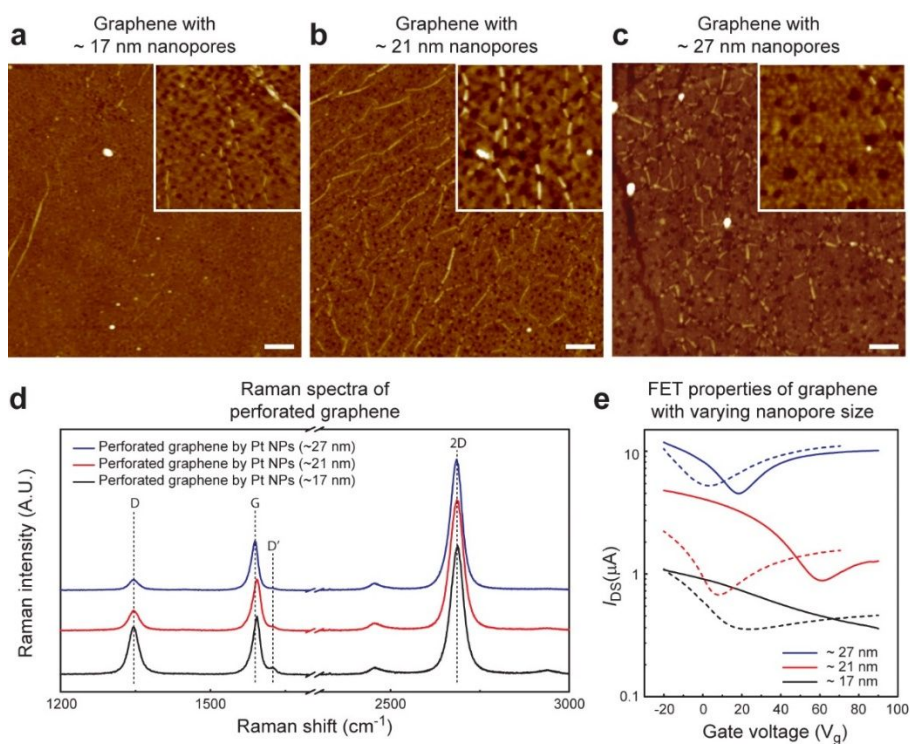


Figure 4. (a) AFM image of nanopores (diameter: 17 nm, spacing: 42 nm) of CVD graphene obtained from smaller molecular weight of diblock copolymer PS-P4VP (32k-13k). (b) AFM image of nanopores (diameter: 21 nm, spacing: 56 nm) of CVD graphene obtained from diblock copolymer PS-P4VP (51k-18k). (c) AFM image of nanopores (diameter: 27 nm, spacing: 125 nm) of CVD graphene obtained from higher molecular weight of diblock copolymer PS-P4VP (109k-27k). (d) Raman spectrum with respect to each sample. (e) I_{ds} of each sample measured at constant $V_{ds}=10\text{mV}$ after the annealing under H_2/Ar atmosphere at 300°C for 10 min (solid curves) and 20 min (dashed curves).

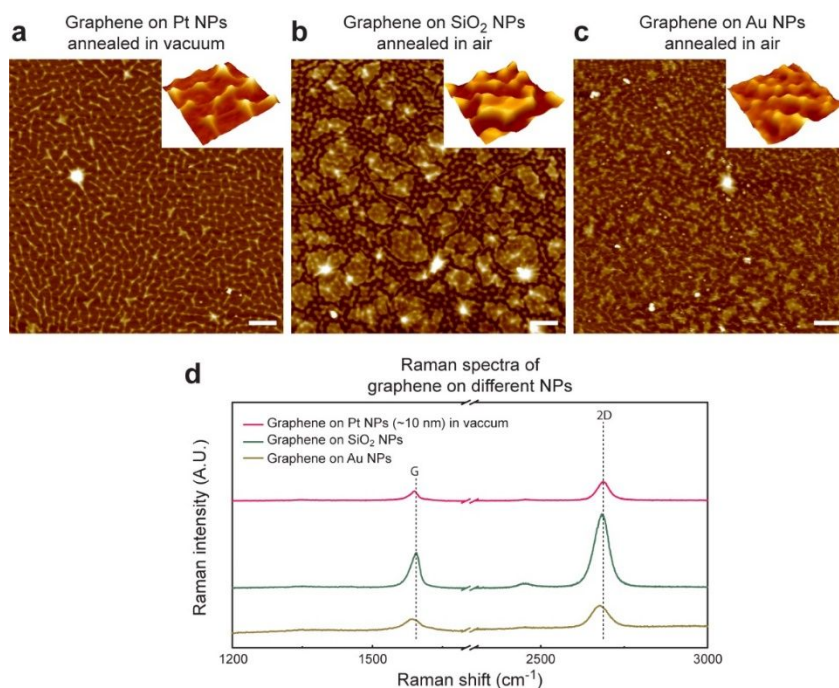


Figure 5. (a) AFM image of annealing treated CVD graphene on Pt NPs in vacuum. (b) AFM image of annealing treated CVD graphene on silica NPs in the air. (c) AFM image of annealing treated CVD graphene on Au NPs in the air. Scale bars are 200 nm. (d) Raman spectrum with respect to each sample.

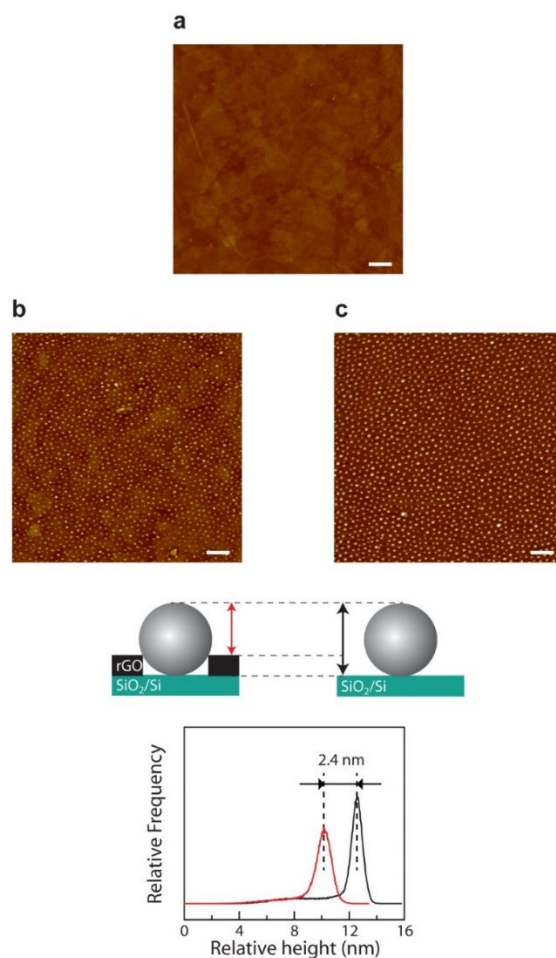


Figure 6. AFM studies of perforated of rGO. (a) AFM image of the spin-coated rGO on SiO₂/Si substrate. (b) AFM image of the arrayed Pt NPs with perforation of rGO film after annealing treatment. (c) AFM image of the Pt NPs synthesized on a bare SiO₂/Si substrate. The height histogram of Pt NPs on rGO is compared with that of the Pt NPs synthesized on a bare SiO₂/Si substrate. The height of Pt NPs on rGO is 2.4 nm smaller. This value indicates that the Pt NPs well penetrates the rGO film and resides on the SiO₂/Si substrate. Scale bars are 200 nm.

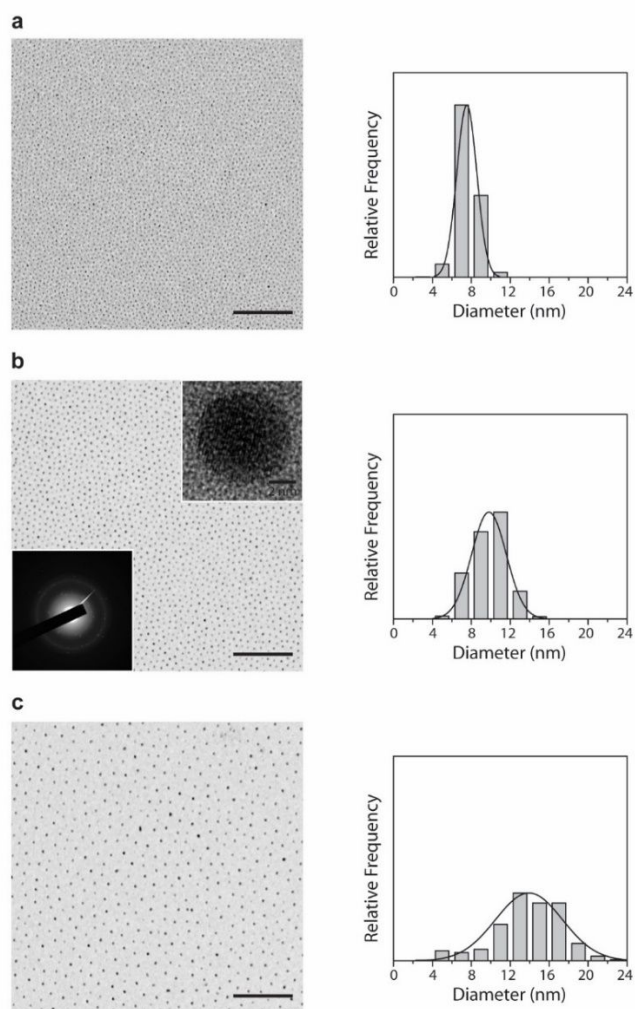


Figure 7. TEM studies of the synthesized Pt NPs. (a) TEM image of the Pt NPs synthesized using the diblock copolymer PS-P4VP (32k-13k). (b) TEM image of the Pt NPs synthesized using the diblock copolymer PS-P4VP (51k-18k). Inset represents the selected-area electron diffraction pattern of Pt NPs. (c) TEM image of the Pt NPs synthesized using the diblock copolymer PS-P4VP (109k-27k). All of the histograms informs the size distribution with respect to each Pt NPs. Scale bars are 500 nm.

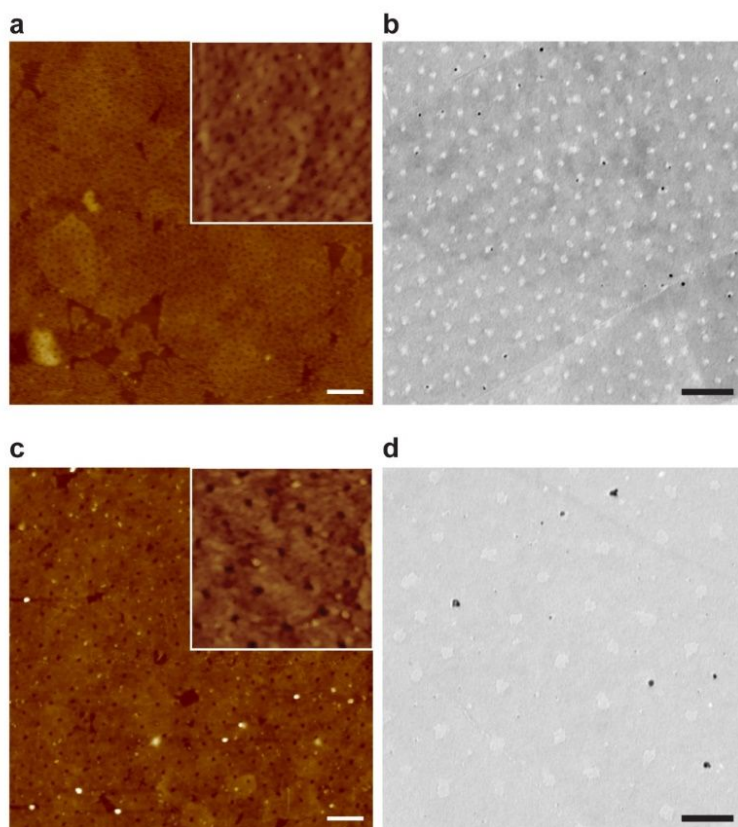


Figure 8. AFM and TEM images of perforated rGO. (a,b) Micrographs of nanopores (diameter: 8 nm, spacing: 34 nm) of rGO obtained from smaller molecular weight of diblock copolymer PS-P4VP (32k-13k). (c,d) Micrographs of nanopores (diameter: 19 nm, spacing: 101 nm) of rGO obtained from higher molecular weight of diblock copolymer PS-P4VP (109k-27k). Scale bars in AFM and TEM images are 200 nm.

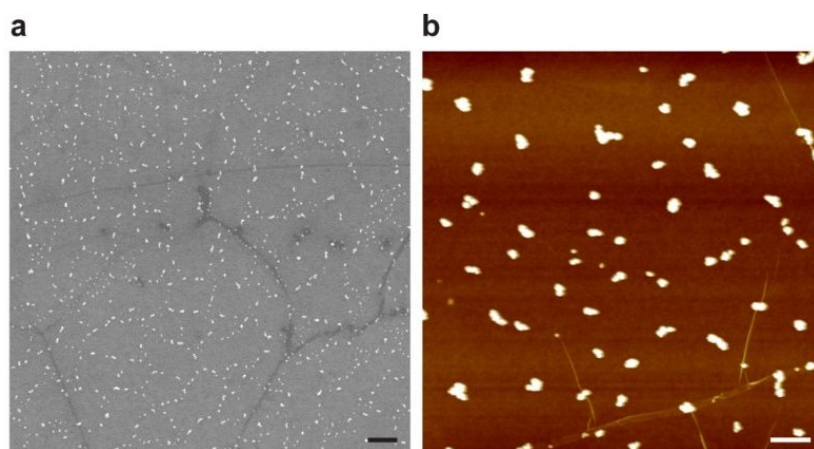


Figure 9. Aggregation of the Pt NPs on CVD graphene. (a) SEM image of the large aggregation of the Pt NPs on CVD graphene forming clusters. (b) AFM image of the aggregation of the Pt NPs on CVD graphene. Scale bars in SEM and AFM images are 200 nm.

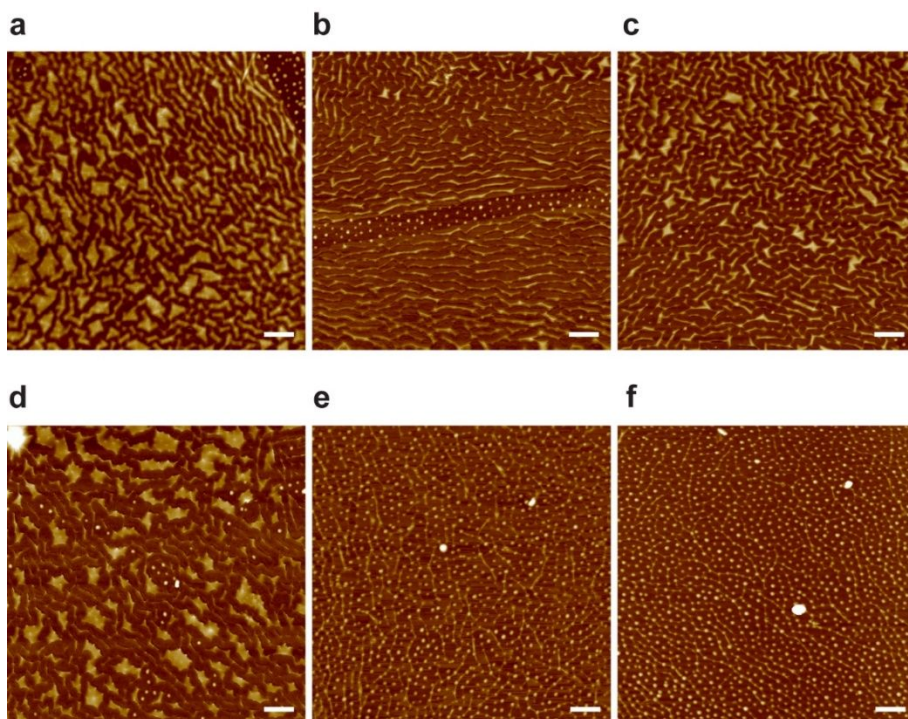


Figure 10. Surface morphology variation of CVD graphene. (a) AFM image of CVD graphene transferred on the Pt NPs array. (b) AFM image of annealing treated CVD graphene for 5 min; (c) 10 min; (d) 15 min; (e) 25 min; (f) 30 min. The ripples coexisted with suspended region are contracted, forming linear creases induced by negative thermal expansion coefficient of graphene. Localized compressive strain of graphene can act as catalytic oxidation sites for Pt NPs to decompose the chemically weakened bonding region. Scale bars are 200 nm.

Table 1. Charge density and strain in graphene on Pt NPs array as a function of annealing.

	Charge density (n)	Strain (ϵ) ^{a)}
On SiO ₂ /Si	$3.55 \times 10^{12} \text{ cm}^{-2}$	$\epsilon_{\text{C}} : 0.15 \%$
0min	$3.8 \times 10^{12} \text{ cm}^{-2}$	$\epsilon_{\text{T}} : 0.16 \%$
10min	$6 \times 10^{12} \text{ cm}^{-2}$	$\epsilon_{\text{C}} : 0.08 \%$
20min	$9 \times 10^{12} \text{ cm}^{-2}$	$\epsilon_{\text{C}} : 0.10 \%$
30min	$1.2 \times 10^{13} \text{ cm}^{-2}$	$\epsilon_{\text{C}} : 0.22 \%$

a) ϵ_{C} : compressive strain, ϵ_{T} : tensile strain

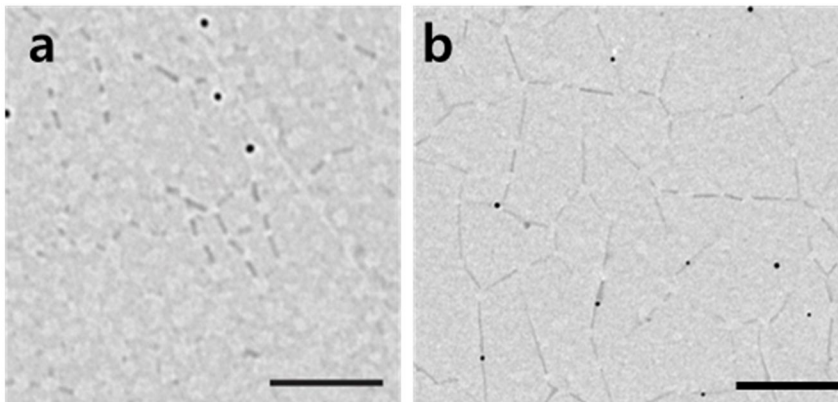


Figure 11. TEM images of perforated single-layer graphene suspended in TEM grids. The single layer thickness of graphene does not give enough contrast to clearly visualize the existence of nanopores. Scale

bars, 200 nm.

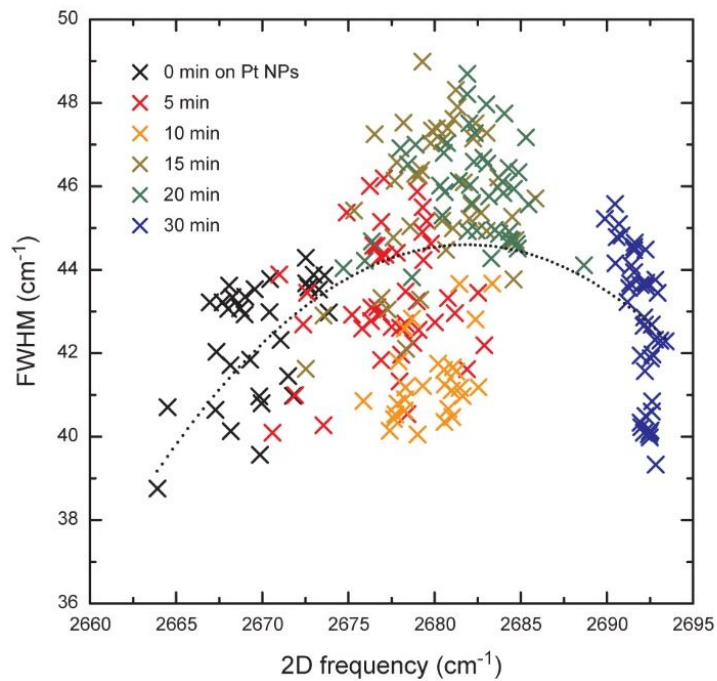


Figure 12. Raman analyses of CVD graphene on Pt NPs with respect to annealing time. Correlation between FWHM of 2D mode and its position as a function of each annealing treated samples (Black dashed line represents the second order polynomial curve fit of whole data points).

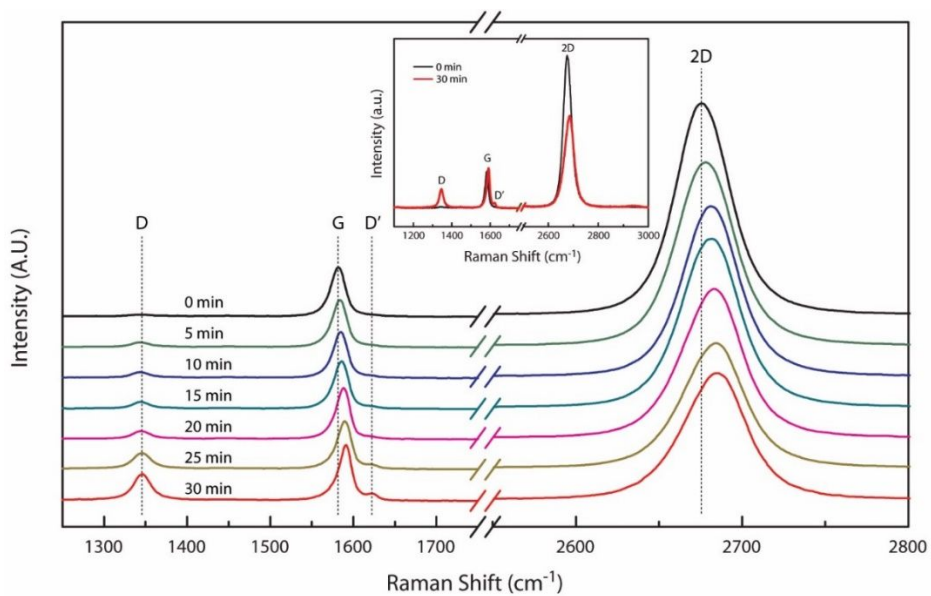


Figure 13. Annealing induced Raman spectrum variation. The D and D' bands are increased proportional to annealing time, which is attributed to sp^2 bond breaking resulting in the formation of nanopore. The blue shift of the G and 2D modes is caused by strong hole doping effect during annealing in the air (Inset represent the raman spectrum variation of before and after annealing. This spectra difference can be an indicator to estimate whether the pores is formed or not).

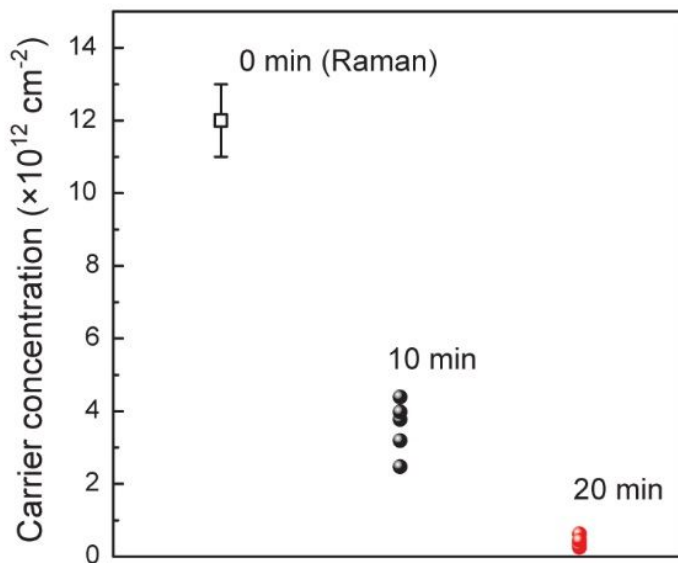


Figure 14. Reduction of the doping concentration by the annealing process. Carrier concentration of the perforated graphene obtained from PS-P4VP (51k-18k) after the annealing at 300 °C under H₂/Ar atmosphere.

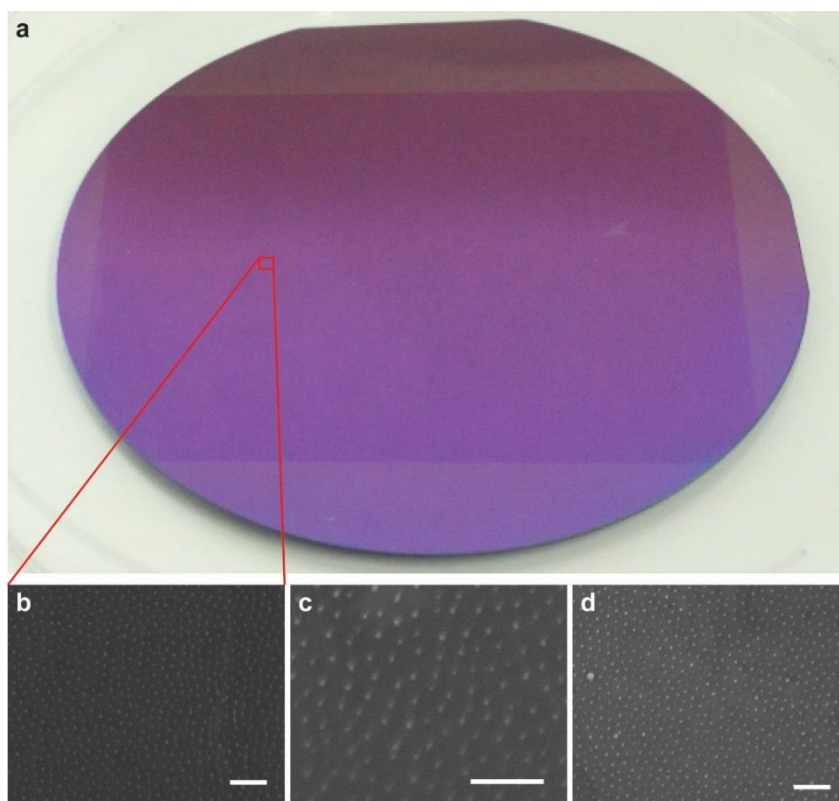


Figure 15. Photograph and SEM images for the perforation of wafer-scale graphene on the arrayed Pt NPs. Photograph and SEM images for the strain-assisted perforation of wafer-scale graphene on the arrayed Pt NPs. (a) Graphene film transferred on Pt NPs arrays on a 4-inch wafer. (b, c). Graphene on Pt NPs before annealing. (d) Perforated graphene on Pt NPs after annealing at 400° C for 30min. Scale bars are 200 nm.

Appendix

A. List of publication

B. List of presentation

A. List of publication

1. Kim, J. K.*; Park, M. J.*; Kim, S. J.; Wang, D. H.; Cho, S. P.; Bae, S.; Park, J. H.; Hong, B. H., Balancing Light Absorptivity and Carrier Conductivity of Graphene Quantum Dots for High-Efficiency Bulk Heterojunction Solar Cells. *ACS Nano* **2013**, *7* (8), 7207–7212.
2. Kim, Y.; Ryu, J.; Park, M. J.; Kim, E. S.; Yoo, J. M.; Park, J.; Kang, J. H.; Hong, B. H., Vapor-Phase Molecular Doping of Graphene for High-Performance Transparent Electrodes. *ACS Nano* **2014**, *8* (1), 868–874.
3. Kim, J. K.; Kim, S. J.; Park, M. J.; Bae, S.; Cho, S.-P.; Du, Q. G.; Wang, D. H.; Park, J. H.; Hong, B. H., Surface-Engineered Graphene Quantum Dots Incorporated into Polymer Layers for High Performance Organic Photovoltaics. *Scientific Reports* **2015**, *5*, 14276.
4. Kyu Kim, J.; Bae, S.; Yi, Y.; Park, M. J.; Jin Kim, S.; Myoung, N.; Lee, C.-L.; Hee Hong, B.; Hyeok Park, J., Origin of White Electroluminescence in Graphene Quantum Dots Embedded Host/Guest Polymer Light Emitting Diodes. *Scientific Reports* **2015**, *5*, 11032.
5. Lee, K. D.; Park, M. J.; Kim, D.-Y.; Kim, S. M.; Kang, B.; Kim, S.; Kim, H.; Lee, H.-S.; Kang, Y.; Yoon, S. S.; Hong, B. H.; Kim, D., Graphene Quantum Dot Layers with Energy-Down-Shift Effect on Crystalline-Silicon Solar Cells. *ACS Applied Materials & Interfaces* **2015**, *7* (34), 19043–19049.

6. Kim, S.-S.*; Park, M. J.*; Kim, J.-H.; Ahn, G.; Ryu, S.; Hong, B. H.; Sohn, B.-H., Strain-Assisted Wafer-Scale Nanoperforation of Single-Layer Graphene by Arrayed Pt Nanoparticles. *Chemistry of Materials* **2015**, *27* (20), 7003–7010.

B. List of presentation

1. Myung Jin Park, Jung Kyu Kim, Sang Jin Kim, Sukang Bae, Jong Hyeok Park , Byung Hee Hong, Enhanced Power Conversion Efficiency of Bulkheterojunction Solar Cells by Addition of Selectively Reduced Graphene Quantum Dots, Nano Korea 2013 Symposium, COEX, Korea, July 10–12, 2013
2. Myung Jin Park, Sung-Soo Kim, Jeong-Hee Kim, Gwanghyun Ahn, Sunmin Ryu, Byeong-Hyeok Sohn and Byung Hee Hong, Nanoscale Perforation of Large-Area Graphene by Arrayed Pt Nanoparticles, The 1st international conference on 2D layered materials, China, Oct., 2014
3. Myung Jin Park, Sung-Soo Kim, Jeong-Hee Kim, Gwanghyun Ahn, Sunmin Ryu, Byeong-Hyeok Sohn and Byung Hee Hong, Strain-Assisted Wafer-Scale Nanoperforation of Single-Layer Graphene by Arrayed Pt Nanoparticles, Graphene week 2014, Sweden, Jun., 2014

국문초록

그래핀 양자점과 반양자점의 합성

박 명 진

화학부 물리화학 전공

서울대학교 대학원

2010년 노벨 물리학상은 ‘2차원 물질인 그래핀의 근본적 돌파구를 제시한 실험에 대한 공로’로 안드레가임, 콘스탄틴 노보셀로프 교수에게 공동으로 수여되었다.

그래핀 연구는 예전부터 탄소나노튜브, 풀러렌을 연구하던 과학자들에 의해 자연스럽게 연구되었고, 새로운 유행으로 발전되었다. 그래핀 연구를 위한 분석장비로는 투과전자현미경, 주사전자 현미경, 전자소자를 이용한 분석, 라만분광법등이 쓰이고 있는데 이는 탄소나노튜브에서 쓰이던 방법과 매우 비슷하다. 이러한 유사점들은 그래핀의 새로운 현상을 이해하는데 빠른 기회를 창출해주었다.

같은 탄소계열인 풀러렌, 탄소나노튜브와 그래핀의 가장 큰 차이점이라면 샘플 제작 측면을 들 수 있을 것이다. 풀러렌은 도펀트를 첨가하거나 작용기를 도입하기가 용이한 면이 있음에도 불구하고 최종화합물을 정제하는데 시간이 오래 걸리고 대량합성이 어려운 단점이 있다. 탄소나노튜브의 경우 혼성화된 분자 비대칭성 때문에 반도체와 도체의 동시다발적인 역할로 인해 전자기적 특성을 방해한다는 문제가 지적되고 있다.

반면 그래핀은 이러한 제조문제를 화학증기증착법, 화학적 박리법, 기계적 박리법 등 다양한 합성법으로 해결한 듯 보여진다. 이를 통해 싸고, 질 좋은 그래핀의 합성이 가능해졌고 다양한 분야에 적용할 수 있게 되었다.

그래핀은 디락포인트에서 원자가 전자대와 전도대가 만나 제로밴드갭을 갖고 있는 물질이다. 이 지점에서는 전자상태밀도가 0이된다. 이러한 밴드구조는 매우 특이한 전자수송특성을 보여준다. 전하운반자가 무한대이기 때문에 전하속도가 굉장히 빠르고, 이러한 점은 그래핀이 논리회로보다 고주파대 전자소자에 유력한 후보군이 될 수 있음을 말해준다.

이렇게 많은 관심을 받고 있는 그래핀의 전자구조는 뛰어난 성질을 갖고 있음에도 불구하고 이러한 근본적 특성(제로밴드갭)때문에 밴드갭을 여는 부분이 가장 큰 과제로 여겨진다. 이와 관련하여 최근 그래핀을 0차원으로 줄이는 연구가 많은 관심을 받고 있다. 무수히 많은 이론적 연구결과를 통해 그래핀은 엷지형태와 폭 길이에 따라 밴드구조가 영향을 받는다는 사실이 알려졌다. 첫 번째 실험적 연구결과는 전자 빔 리소그래피 공정을 이용하여 제작된 그래핀 나노리본이었다. 측정된 밴드갭은 그래핀 나노리본의 폭과 반비례하는 경향을 보였다. 그러나 이러한 리소그래피 공정은 10nm이하의 패터닝 한계가 있다. 이러한 문제를 극복하기 위하여 화학적 방법을 이용한 박리법이 개발되었고, 더 작고, 좁은 폭을 가지며 모양과 재현성이 가능한 그래핀 나노리본제작이 가능해졌다. 그래핀 나노리본과 관련하여 그래핀 나노메쉬가 있는데, 이는 주기적인 구멍배열로 이루어져 있으며, 구멍사이의 간격이 5nm로 좁기 때문에 보다 더 쉽게 밴드갭을 열 수가 있다.

이 논문은 그래핀 나노리본과 비슷한 특성을 갖는 그래핀 양자점과 그래핀 나노메쉬의 제작법, 그리고 이렇게 제작된 나노구조체의 응용에 대한 소개를 주제로 한다.

먼저 소개하기에 앞서 그래핀의 이해를 돕기 위해 전반적인 소개를 먼저

할 것이며, 이 후에 2장과 3장에서 구체적인 연구내용을 소개할 것이다.

주요어: 그래핀, 그래핀 양자점, 그래핀 나노메쉬, 반도체, 그래핀 라만, 광학변이

학번 : 2012-23043